Analyzing induced seismicity using the techniques of observational seismology: A case study of a hydraulic fracturing operation in northeast British Columbia

by

Chet Goerzen
B.Sc., University of Victoria, 2021

A Thesis Submitted in Partial Fulfillment of the
Requirements for the Degree of

MASTER OF SCIENCE

in the School of Earth and Ocean Sciences

We acknowledge and respect the Lək̓ʷəŋən (Songhees and Esquimalt) Peoples on whose territory the university stands, and the Lək̓ʷəŋən and W̱SÁNEĆ Peoples whose historical relationships with the land continue to this day

Analyzing induced seismicity using the techniques of observational seismology: A case study of a hydraulic fracturing operation in northeast British Columbia

by

Chet Goerzen
B.Sc., University of Victoria, 2021

Supervisory Committee

Dr. Honn Kao, Co-Supervisor
School of Earth and Ocean Sciences

Dr. Stan Dosso, Co-Supervisor
School of Earth and Ocean Sciences

Dr. Blake Dyer, Departmental Member
School of Earth and Ocean Sciences

Abstract

This thesis uses techniques of observational seismology to investigate induced seismicity related to a hydraulic fracturing operation. The hydraulic fracturing operation targeted the Montney formation in the Western Canada Sedimentary Basin. This study is unique due to its unprecedented resolution in both seismic data and injection information. An initial earthquake catalog is developed, with 3377 high quality events detected from 2021-01-26 to 2021-06-06. Joint high precision double difference earthquake relocation and tomography are performed. The majority of earthquakes in the catalog were associated with the Tower Lake hydraulic fracturing operation. The study area is located near Taylor, British Columbia, and the hydraulic fracturing operation was targeting the Montney formation for the extraction of oil and gas resources. It is found that the cumulative injected fluid volume is the injection parameter with the most influence on seismicity. Injection pressure and rate have less of an effect. This is consistent with the observations that most earthquakes are likely triggered by pore pressure diffusion, rather than the poroelastic effect. Double couple focal mechanisms are also calculated for select earthquakes. The calculated focal mechanisms are generally consistent with the maximum horizontal shear stress in the area. Some small-scale faults are identified using earthquake locations and focal mechanisms. Foreshock sequences are observed along two of the identified faults, demonstrating that fault characterization may be used to help guide injection operations to avoid induced seismicity.

Table of Contents

List of Tables

List of Figures

Acknowledgments

I thank my supervisors Dr. Honn Kao and Dr. Stan Dosso for their support during my masters program. I would also like to thank Ryan Visser for providing the first version of the earthquake catalog in this study. I also benefited from productive discussions with many current and former members of the seismology group at the Pacific Geoscience Centre. I would also like to thank my friends and family for their support throughout my schooling.

Acronyms

DWS: Derivative Weighted Sum
EOR: Enhanced Oil Recovery
GFT: Goodness of Fit Test
GNSS: Global Navigation Satellite System
G-R: Gutenberg-Richter
HF: Hydraulic Fracturing
IIE: Injection Induced Earthquakes
LVZ: Low Velocity Zone
M: Magnitude
MAXC: Maximum Curvature
MOC: Magnitude of Completeness
NEBC: North-east British Columbia
RMS: Root Mean Square
SNR: Signal to Noise Ratio
WCSB: Western Canada Sedimentary Basin
WD: Waste Water Disposal

1. Introduction

This thesis studies induced seismicity triggered by a hydraulic fracturing (HF) operation in northeast British Columbia. The techniques of observational seismology are used to investigate the relationship between HF injection parameters and induced seismicity. Additional analysis is also performed to make observations about the subsurface.

The structure of the thesis is as follows. An introduction to the subject material is provided. The data and methods used for this study are then explained. After this the results are presented, as well as further analysis of the results. Finally, the results and their implications are discussed. The thesis is summarized by the Conclusions section.

1.1 Induced Seismicity

Induced seismicity is any seismicity that is caused by anthropogenic activities. Such activities may include reservoir impoundment, mining, or oil and gas activities. Several different kinds of oil and gas activities may trigger seismicity. These include HF, wastewater disposal (WD), and enhanced oil recovery (EOR). HF triggered seismicity is the main focus of this thesis.

HF is the injection of high-pressure fluids into the subsurface to enhance oil and gas extraction. This high-pressure fluid injection creates small fractures in the oil/gas bearing formation, with the aim being to increase the permeability of the formation. HF operations are often completed in many stages. HF operations start at the toe of the well, and then proceed inwards towards the heel of the well (Figure 1.1). WD is similar to HF, although the purpose of WD is to dispose of waste fluids in the sub-surface. WD operations are typically completed in a vertical well, without any horizontal stages.

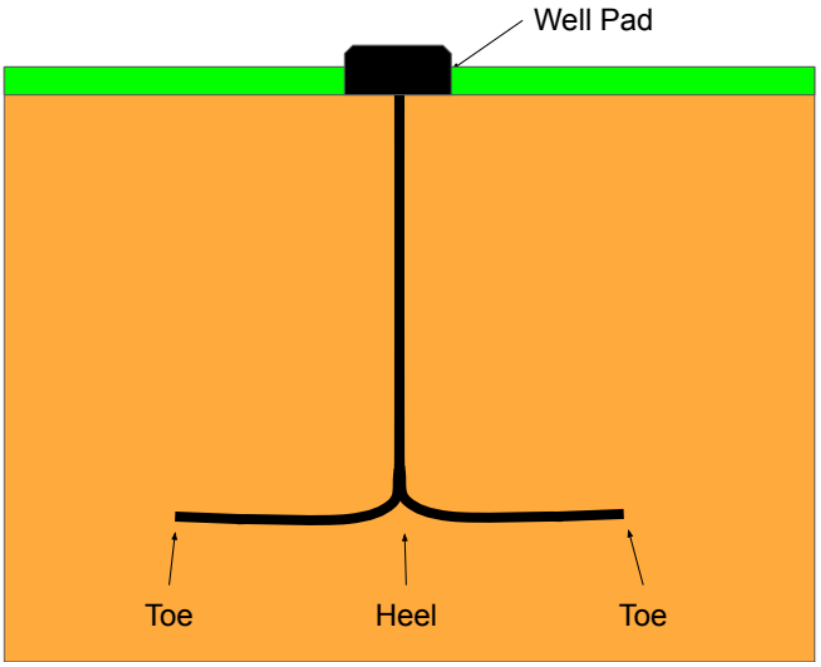

Figure 1.1: Cartoon schematic of a hydraulic fracturing operation.

It has been well established in the literature that subsurface fluid injection can trigger earthquakes (Hubbert & Rubey, 1959; McGarr, 1976). Raleigh et al. (1976) observationally established that earthquakes could be induced by subsurface fluid injection in the Rangely earthquake experiment. The Rangely earthquake experiment was performed at an oil field in Rangely, Colorado, with the goal of investigating the effects of changing fluid pressure on seismicity.

There are three main mechanisms that have been suggested to explain the triggering of induced seismicity. The first, and most commonly accepted mechanism of triggering injection-induced earthquakes (IIE) is the subsurface pore pressure increase due to injection. The theoretical framework for the effect of pore pressure on earthquake initiation was established by the effective stress law of Hubbert & Rubey (1956). As pore pressure increases, the effective normal force to the fault plane is decreased. According to the Mohr-Coulomb failure model, slip can be initiated when the shear stress exceeds the critical shear strength (τ_{crit}), defined as:

$$\tau_{crit} = (S - p)\tan\phi \quad (1)$$

where S is the component of total stress that is normal to the fault plane, with units of megapascals, p is the pore fluid pressure in megapascals, and ϕ is the angle of internal friction. As shown in Equation 1, the critical stress can be as low as zero if S is equal to p. Triggering by pore pressure increase is a fundamental assumption of the McGarr (1976) relationship, where seismic moment release is linearly related to injected volume.

The second possible mechanism to explain IIE is the poroelastic effect. The theory of poroelastic stress changes was established by Biot (1941). In the context of induced seismicity, when fluid is injected into the subsurface, the volume change creates a stress that is propagated through the subsurface medium poroelastically. This stress change may trigger IIE if the fault plane is oriented in such a way that the stress change pushes the fault closer towards failure. Several other researchers have postulated poroelastic effects to explain IIE that have occurred before an increase of pore pressure would have been expected (Li et al., 2021; Yu et al., 2019; Zhai et al., 2019). In theory, the poroelastic stress change can travel at the wave propogation speed in the medium, while pore pressure changes can only travel at the rate of diffusion.

A third mechanism used to explain the existence of IIE is fault lubrication. This mechanism has been observed in laboratory settings (Dou et al., 2020), but is not commonly accepted as a triggering mechanism for in-field IIE.

1.2 Regional Geological Setting

The study area is located in the Western Canada Sedimentary Basin (WCSB). The WCSB is the foreland basin associated with orogeny in the Canadian Cordillera (Porter et al., 1982),

and overlays Precambrian crystalline rocks of the North American craton (Price, 1994). The thickness of the WCSB varies from 0 km to approximately 5 km (Price, 1994). The WCSB is composed of seven main geological features. These include the Montney and Duvernay formations, the Alberta Deep Basin, Williston Basin, Liard Basin, Horn River Basin, and the Cordova Embayment (Figure 1.2).

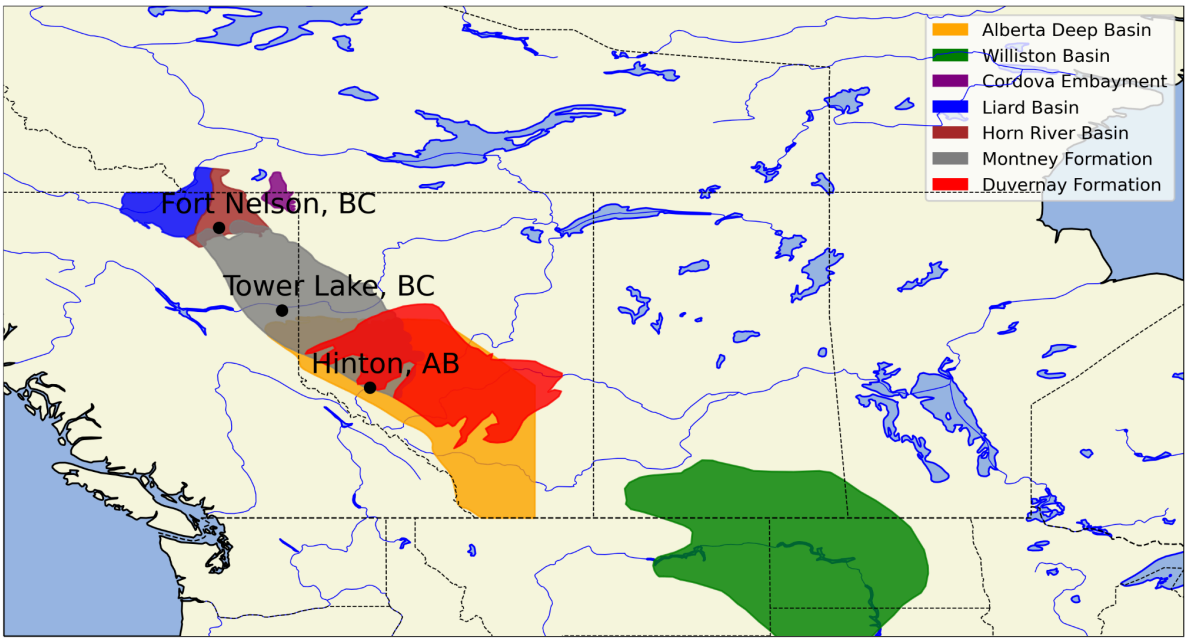

Figure 1.2: Major geological features in the WCSB.

The specific formation that the HF operation in this study targets is the Montney formation, located in northeastern British Columbia and Alberta. The Montney formation roughly extends from Hinton, Alberta, to Fort Nelson, British Columbia. The Montney formation is formed of Triassic age sediments, and has a maximum thickness of 350 m. The Montney and Duvernay formations are the main target formations for unconventional oil and gas operations in the WCSB. The Montney formation is made up of three stratigraphic subunits. These are the Upper, Middle, and Lower Montney subunits. The Middle Montney formation can be further subdivided into Upper Middle and Lower Middle Montney subunits. The Lower Middle Montney formation has been found by Wang et al., 2022 to be more seismogenic than the other subunits.

1.3 Induced Seismicity in British Columbia

IIE have been observed in northeastern British Columbia (NEBC) as early as the 1980s (Horner et al., 1994). Approximately 28,000 oil and gas wells have been drilled in NEBC since the 1950s, according to the BC Energy Regulator (https://www.bc-er.ca/what-we-regulate/oil-gas/). Since 2005, most of the oil and gas development activity in British Columbia has been associated with unconventional resources where conventional vertical wells are not used to extract the hydrocarbons.

While the first IIEs were observed in the 1980s (Horner et al., 1994), it wasn't until 2015 that a link was established between HF and IIE in NEBC by Farahbod et al. (2015) in the Horn River Basin. This link was expanded to the rest of NEBC in a study by Atkinson et al. (2016), who found that 93% of the earthquakes greater than magnitude (M) 3 from 2010-2015 were related to either WD or HF in the WCSB. In the same study, approximately 1.3% of earthquakes in the WCSB from 1985 to 2009 were associated with oil and gas operations, including WD and HF. From 2000 until the end of 2020, over 20,000 seismic events were detected in NEBC (Visser et al., 2021). The studies by Farahbod et al. (2015) and Atkinson et al. (2016) suggest that many of these detected events are IIE.

There are also many WD operations in NEBC (Figure 1.3). Despite the abundance of WD operations, it has been found by many researchers (Atkinson et al., 2016; Wang et al., 2022; Eaton & Schultz, 2018) that seismicity is less susceptible to triggering by WD than HF in NEBC. In contrast to NEBC, IIE in the United States is predominantly triggered by WD although some instances of HF-triggered IIE have been observed (Skoumal et al., 2018).

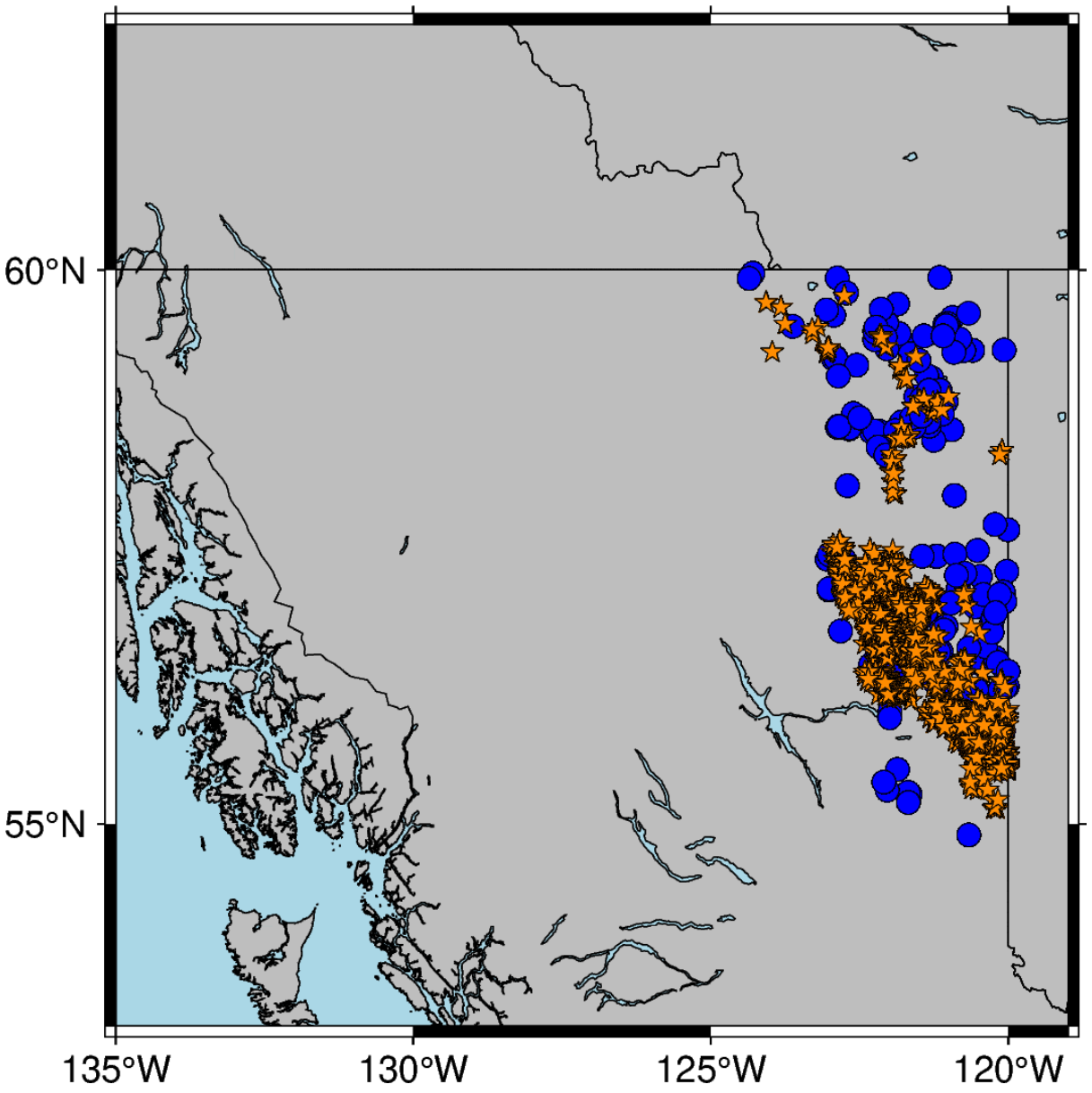

Figure 1.3: WD (blue circles) and HF (orange stars) operations in NEBC from 2013 to 2022.

1.4 Tower Lake Project

The Tower Lake Project is a partnership among Natural Resources Canada, Innovation Solutions Canada, BC Energy Regulator, and two private companies, Symroc and Ovintiv Canada (British Columbia Energy Regulator, 2020). An array of 36 seismic stations was deployed around a HF well near Tower Lake, BC (shown in Figure 1.4). This dense seismic array was in operation from 2021-01-26 to 2021-06-06 and is the main data source for this study. Each station was equipped with one three-component Symroc broadband

seismometer sampling at a rate of 1000 Hz. In order to increase the number of possible observations, the data from 37 nearby stations belonging to 5 pre-existing regional and local seismograph networks were incorporated, including the networks 1E, CN, EO, PQ, and XL. Two selection criteria were used to determine which seismic stations to include in the analysis. First, the station must have been located between 55.6 to 56.2 ° N, and 121.0 to 120.0 ° W, meaning that the furthest seismic station was approximately 50 km away from the HF well. Second, the seismic station must have been active during the Symroc array deployment timeline. A complete list of seismograph stations used in this study, including their locations and sampling rates, is given in the supplemental spreadsheet of this thesis.

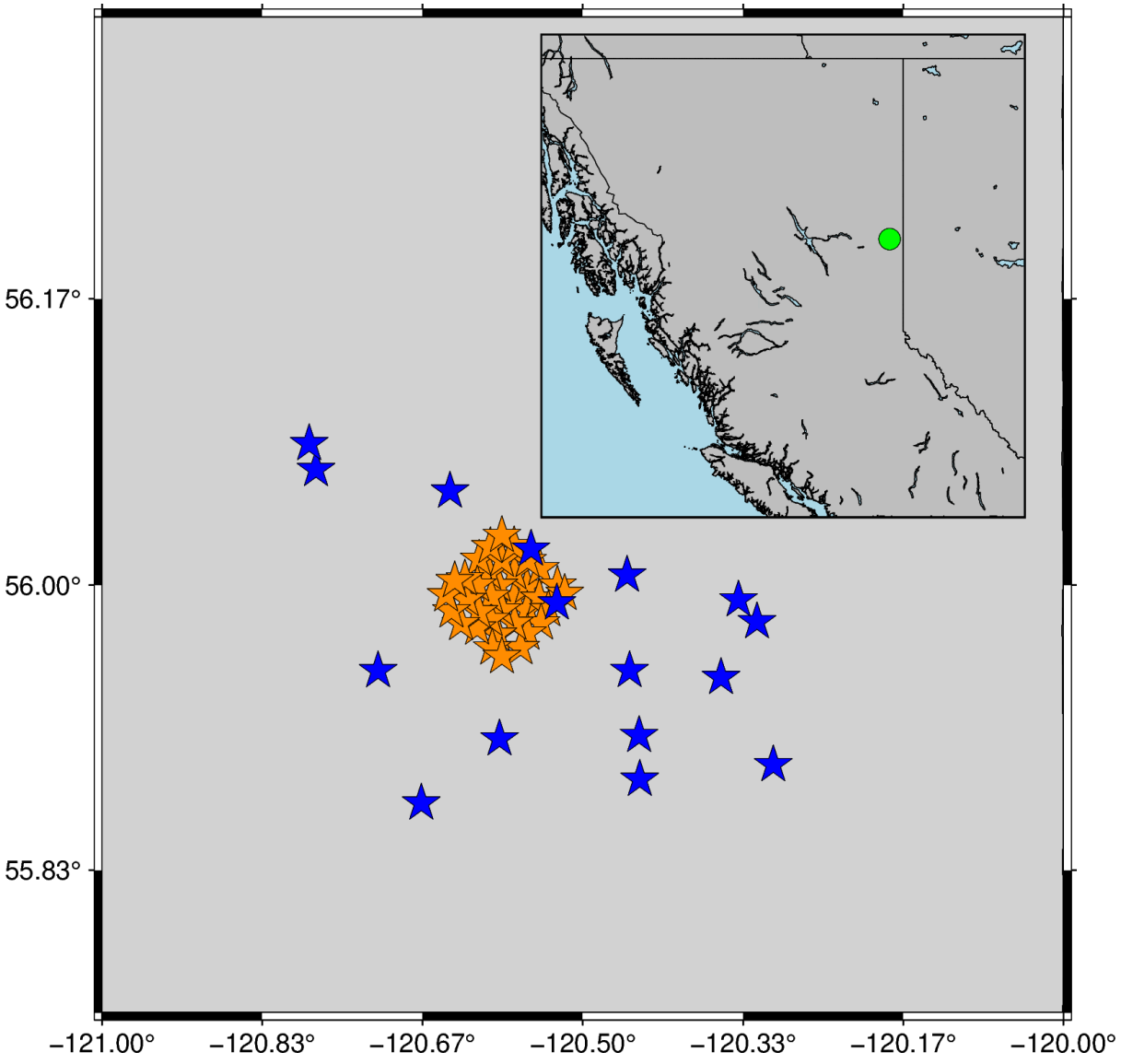

Figure 1.4: Map of the study area and surrounding regions. The green circle is the location of the study area, orange stars denote the locations of Symroc seismic stations, and blue stars denote the locations of other seismic stations used in the analysis.

The Tower Lake HF operation targeted the Montney formation including, at various times, all of the Lower, Middle, and Upper Montney. Injection operations were active from 2021-03-27 to 2021-04-18. An eight well HF configuration was employed. The closest B-ranked (meaning that the stress azimuth measurement was accurate to within 20°) stress measurement to the Tower Lake HF operation is a bore-breakout measurement at 0.60 km depth (Heidbach et al., 2018). Bore-breakout measurements are performed by measuring the deformation of a drilled borehole. The measured maximum horizontal compressive stress direction (S_{Hmax}) was 43° clockwise from north in this area. Several other stress measurements in the area are consistent with this observation (Table 1.1).

Table 1.1: A selection of stress measurements from the World Stress Map (Heidbach et al., 2018). The nearest four measurements to the Tower Lake HF well are listed. Quality rankings are as described in Heidbach et al. (2018). S_{Hmax} is measured in degrees clockwise from north.

S_{Hmax} (°)	Latitude (°N)	Longitude (°E)	Depth (km)	Quality	ID code
43	56.528	-120.565	0.60	B	wsm20786
42	55.992	-120.738	0.55	D	wsm20929
40	56.224	-120.328	0.80	C	wsm20888
55	56.107	-121.207	0.35	D	wsm20891

2. Data and Methods

2.1 Determination of Earthquake Source Parameters

There are several parameters used to describe an earthquake that are useful for induced seismicity research. These parameters include hypocentral location, origin time, and magnitude. The methodology used to calculate these parameters is outlined in the following sections.

2.1.1 Timing Correction

A one-second time offset relative to the regional stations was systematically observed in the data from the Symroc array. This was caused by an issue with the satellite communication to the Symroc array (Symroc personal communication, 2023). Specifically, the disruption in satellite communication caused the Global Navigation Satellite System (GNSS) calibrated timing information to be offset by one second. Fortunately, this timing offset was consistent throughout the Symroc array. This timing error was corrected by shifting the timestamps of the Symroc data by one second to match the timing of the regional stations.

2.1.2 Phase Picking

Measuring earthquake phase arrival times is an essential step towards calculating earthquake source parameters. The EQTransformer machine learning model (Mousavi et al., 2020) was employed for that purpose. An in-depth study was performed by Pita-Sllim et al. (2023). That study found that the EQTransformer detector was highly sensitive to input parameters, and that the model often made incorrect phase picks when secondary phases were present. The parameters selected in this study were decided using extensive

experience with the EQTransformer model in routine operations. Additionally, due to the local small scale of the study area, secondary phases are not commonly observed. EQTransformer consists of two modules. In the first module, the entire waveform database is scanned, and waveform segments with a high probability of containing energy from an earthquake are identified. Once potential earthquake segments are identified in the waveform dataset, these segments are analyzed to identify potential phase arrivals using the second module of EQTransformer. This module outputs the probability of either a P- or S-wave phase arrival, for the entire detection window. The phase prediction probabilities do not necessarily represent the model confidence that a phase exists at a certain timestamp, but rather the probabilities are related to the model output that attempts to recreate the labels of the training dataset. The EQTransformer model used in this study was fine-tuned for NEBC based on previous analyst-measured earthquake phase arrival times. In order to ensure high-quality arrival time measurements, several different probability thresholds were employed. For the event detection module of EQTransformer, the model must predict a probability of 0.1 or greater for a waveform segment to be classified as an earthquake detection. For the phase picking module of EQTransformer, the model must predict a probability of 0.08 or greater for a waveform segment to be classified as a phase detection. The timestamp with the greatest probability within the phase picking window is accepted as the arrival time.

2.1.3 Phase Association

Once the seismic phase detection has been completed, it is essential to associate each seismic phase with a seismic event. It is not immediately apparent which seismic event a given seismic phase may be associated with, especially when multiple seismic events occur close in time. However, using theoretical travel times calculated for different phases, it is possible to identify which phases are likely associated with the same event. A coarse grid is defined over the study area. This grid extends from 120.8° to 120.2°W, and 55.75° to 56.2°N. The grid spacing is 0.1° in both latitude and longitude and is also centered at 1 km

depth. Theoretical travel times are then calculated for each possible source and receiver pair. The possible sources can be anywhere on the initial travel time grid, while the possible receiver locations are the seismic station locations. The 1D velocity model of Mahani et al. (2021) is used to calculate theoretical travel times. For each phase detected by EQTransformer, all other P- and S-phases within a specified time window are selected. No secondary phases were considered. This time window is calculated as the maximum possible S-wave travel time in the area, plus 20 s. Then, for each grid node in the study area, all arrival times for a given set of phases are back-projected using the theoretical travel time grid. This yields an estimated origin time at each grid node for a given phase. If the back-projected origin time of at least seven phases falls within a 4-s time window at any grid node, this grid node is considered a preliminary solution. If several grid nodes exceed this threshold, the grid node with the maximum number of associated phases is selected.

2.1.4 Location

The NonLinLoc algorithm (Lomax et al., 2000) was employed to perform the earthquake location inversion. Solution space sampling is performed by the Oct-tree algorithm (Lomax & Curtis, 2001) which is a way of recursively sampling the solution space, guided by the probability density function of the earthquake location. A grid with 160 cells in each horizontal direction, and 5 cells in the vertical direction is initialized for the Oct-tree algorithm. The minimum node size is set to 1×10^{-6}°. The maximum number of nodes is 1.3×10^{5}, and 1.0×10^{5} scatter samples are drawn. The equal differential time location method (Font et al., 2004) is employed, with travel time calculations performed using the Mahani et al. (2021) velocity model. The equal differential time location algorithm is a method of calculating the probability density function of the earthquake location on a grid, using differential travel times between different seismic stations for a given event. Four phases must be used in the earthquake location calculation for an earthquake location solution to be selected.

2.1.5 Magnitude Calculation

Earthquake magnitudes are a useful parameter for induced seismicity research. In this thesis amplitudes are measured from the earthquake waveforms. The amplitudes are then used to calculate earthquake magnitudes. Because the amplitude measurements are made on the earthquake waveforms, it is essential to have a reference point to make these measurements. Each phase arrival time measurement is used as a reference point for making an amplitude measurement. All amplitude measurements are made using vertical-component seismic recordings. Several pre-processing steps were performed before making the magnitude estimates. The time series data are first detrended by removing the linear trend between the first and last sample of the seismic data. The mean of the data is subtracted from the data, such that the new mean of the data is zero. Next, a highpass filter with a corner frequency of 0.3 Hz and three corners is applied. This means that the filter is applied both forwards and backwards three times, for a total of six applications of the filter. A time window extending from 20 s before to 30 s after the phase pick is selected for instrument response removal. The instrument response is then removed using the Obspy (Beyreuther et al., 2010) instrument response removal functionality. The data after response removal are in units of meters per second. A water level of 1 dB is applied during the response-removal (deconvolution) process. Then, the instrument response of a Wood-Anderson seismometer is simulated, in units of meters. The Wood-Anderson seismometer response is chosen to be consistent with Mahani & Kao (2018). A short time window is then selected around the phase pick. Both P- and S-phase measurements are used to define the time window. For a P-phase arrival time measurement, a theoretical S-phase arrival time estimate was made, and vice versa. The start of the window is calculated as:

$$t_{start} = t_s - \frac{1}{2}\left(t_s - t_p\right) \quad (2)$$

where t_s is the S-wave arrival time, and t_p is the P-wave arrival time. The end time of the window is calculated as:

$$t_{end} = t_{start} + 2 \times \left(t_s - t_p\right) \quad (3)$$

The minimum length of the window is 2 s. If the calculated time window is less than 2 s, the window is calculated as the P-phase arrival time plus 2 s. In addition, the time series data must have an absolute value of less than 0.5 mm at some point in the time window for a magnitude measurement to be made. This is to ensure that there is at least one zero-crossing in the data, and is a way of checking that the data are valid. The amplitude is calculated as the maximum absolute value of the data in the time window. To calculate magnitude values from amplitude measurements, Equation 3 from Mahani and Kao (2019) is used, with the parameters derived from that study. The median value of the magnitude estimates from all stations for a given earthquake is used for the earthquake's magnitude. The standard deviation about the mean of all magnitude estimates for an earthquake is calculated to estimate uncertainty. Earthquake magnitude results are considered further in Sections 3.2, 3.4, and 4.2.

2.1.6 Focal Mechanism Calculation

Earthquake focal mechanisms provide information on both the earthquake fault rupture, as well as the regional stress field of the area that an earthquake occurred. In order to calculate a focal mechanism, first motion earthquake phase polarity measurements must be made at a number of seismic stations surrounding the epicenter. In this thesis, first motion measurements were made manually. In order to facilitate the measurement of phase polarities, the Snuffler (Heimann et al., 2017) software was employed. Due to the large number of seismic events recorded, it was not feasible to measure first motion polarities for the entire earthquake catalog, so a subset of earthquakes was selected to be analyzed. Our

selection criteria for making first motion polarity measurements were that an earthquake must have recorded phase arrivals at a minimum of 45 seismic stations, and the earthquake must have occurred after the commencement of the Tower Lake injection operations. In order to make accurate and precise first motion polarity measurements, several pre-processing steps were employed. First, the instrument response was removed. Then, a bandpass filter with a low corner frequency of 1 Hz and a high corner frequency of 25 Hz was applied. The Symroc stations had a 180° polarity reversal in the 1 Hz to 10 Hz frequency band (Dr. Hongyu Yu, personal communication, Nov 6, 2023). To correct for this, the sign of the first motion polarity measurements was reversed for the Symroc stations. The first motion polarity measurements were then inverted for a double-couple moment tensor using the Bayesian Earthquake Analysis Tool (Vasyura-Bathke et al., 2020). The custom velocity model of Mahani et al. (2021) was used in the inversion. The focal mechanism results will be considered further in Section 3.4.

2.2 Double Difference Tomography and Hypocentral Relocation

In order to acquire high-precision earthquake locations, the double difference tomography and hypocentral relocation software TomoDD (Zhang & Thurber, 2006) was employed. Double difference relocation represents a significant improvement over conventional earthquake location techniques. Instead of simply using absolute arrival time measurements, double difference techniques use the difference in travel times between event pairs. It is required that the distance between events in the event pair is much smaller than the distance between the event pair and the receiver, so that the inversion is sensitive to differences in earthquake location, rather than variations in earth properties along the seismic ray path. Combined with absolute travel time measurements from the initial catalog, double difference techniques can provide extremely high precision earthquake locations. In addition, TomoDD also inverts for perturbations to the initial velocity model used to determine earthquake locations. Because earthquake location estimates depend on the

velocity model used for location, improving the velocity model can increase the accuracy of earthquake locations.

Several steps were required to prepare the data for TomoDD. The first step was earthquake selection. All events that had passed the location quality control criteria were considered for analysis. Only the vertical components were used for calculating cross-correlation differential times. A window around the P-phase arrival time was selected, starting 0.2 s before the P-phase arrival and ending 0.8 s after the arrival. Because the cross-correlation measurements were made between waveforms from the same seismic station, the instrument response was not removed from the waveforms, assuming that the instrument response of the seismometer does not change over time. A bandpass filter from 1 Hz to 10 Hz was applied. In order for a cross-correlation time delay to be used in the analysis, the cross-correlation value must be greater than 0.6, and less than 0.98. This has the effect of removing low quality measurements, as well as a type of false detection where one event is detected as multiple duplicate events. The TomoDD algorithm also requires absolute travel time measurements from the initial earthquake catalog. These are derived directly from the phase arrival time measurements in the initial catalog. The maximum allowable separation between hypocenters for each event pair was 3 km. Observations at at least eight seismic stations were required for an earthquake pair to be considered for further analysis, with a maximum of 35 observations. The TomoDD results will be considered further in Sections 3.2 and 3.3

3. Analysis and Results

3.1 Initial Earthquake Catalog

The initial earthquake catalog was produced by Ryan Visser, with further iterations being completed by the author. This initial catalog contained 3377 events, as shown in Figure 3.1. The largest estimated magnitude was 2.6, while the smallest was −0.5. The earthquake catalog spans the dates from 2021-01-26 to 2021-06-05. Note that many events seem to be located along the study area boundaries. These events are likely caused by false detections from the EQTransformer software that pass our quality control measures, and are removed from further analysis.

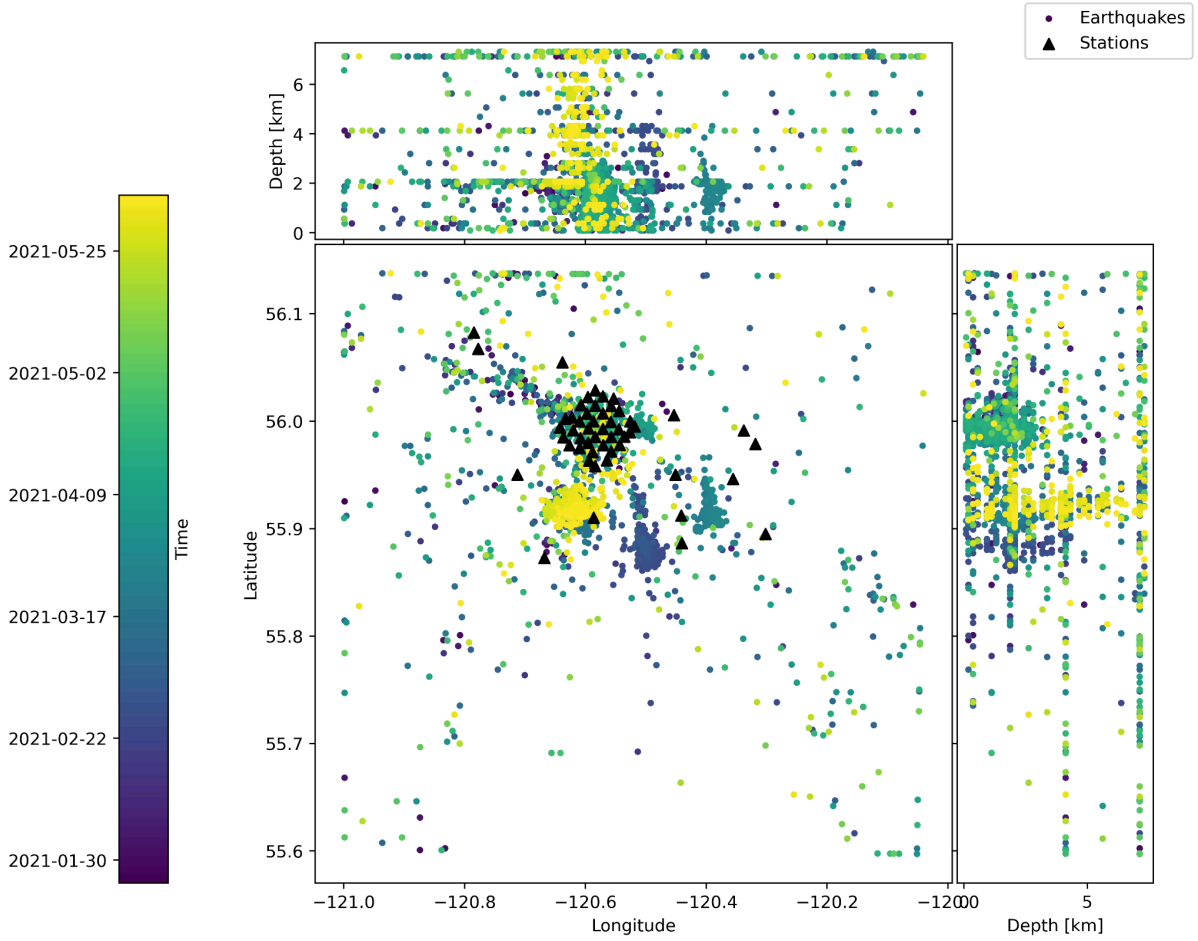

Figure 3.1: Initial earthquake catalog. Events are colored by time of occurrence, as indicated by the color bar. Seismic stations are indicated by black triangles.

There are several parameters that indicate the quality of the earthquake catalog. The greatest number of phases used for earthquake location was 124. The smallest number of phases was 4, which was the minimum required for a solution to be accepted. The smallest RMS residual was 0.0018 s, while the largest RMS residual was 0.91 s. The mean RMS was 0.09 s, and the standard deviation of the RMS was 0.06 s.

3.2 High Precision Earthquake Relocations

Of the 3377 earthquakes in the original catalog, 2193 earthquakes were successfully relocated. This reduction in events is likely caused by the quality control measures required for relocation, rather than events being relocated outside of the study area. For a given event pair, at least eight double difference travel time measurements are required. A number of events in the initial catalog do not meet this threshold. Further, 29 events were removed from the joint earthquake and tomography inversion due to their relocated positions falling outside of the study area. The largest event in the initial catalog was successfully relocated, while the smallest event that was successfully relocated was magnitude -0.48. The magnitude estimates were taken from the initial catalog, without adjusting for the shift in location in the relocated catalog. The mean shift in the east-west, north-south, and depth directions was 69.7, 77.9, and 167.5 m, respectively. Thus, the change in magnitude due to shifts in location should be negligible.

The earthquake catalog was modeled as a Gutenberg-Richter (G-R) distribution in order to provide an estimate of how well small earthquakes were recorded in the dataset. The G-R distribution is a linear relationship between the logarithm of the frequency of seismic events and the earthquake magnitudes, as defined by the following equation:

$$\log_{10}\mathrm{N(M)} = a - b\mathrm{M} \tag{4}$$

where $N(\mathrm{M})$ is the number of events above magnitude M, and a and b are empirical parameters. The G-R model assumes that all events that occurred are actually recorded. The magnitude of completeness (MOC) is an estimate for the smallest magnitude above which all earthquakes that occurred are included in the catalog. Events below the MOC are not included in the G-R modeling. The b-value parameter is the absolute value of the slope of the cumulative magnitude curve. The b-value provides information on how the number of events in an earthquake catalog is dependent on earthquake magnitude. For catalogs with a high b-value, the earthquake occurrence rate drops more sharply with increasing magnitude than a catalog with a low b-value. Typically, b-values for induced seismicity catalogs are greater than one, with a value of 1.37 reported by Mahani (2021) for the Montney formation.

In order to focus on the b-value for earthquakes triggered by the Tower Lake operation, only events within the area bounded by 55.96 - 56.04°N and 120.45 - 120.70°W were selected. The resulting catalog contained 1318 events. Two different methods were used to calculate the G-R parameters. The first method used was the maximum curvature (MAXC) method of Wyss et al. (1999). The MAXC method estimates the MOC by taking the derivative of the $\log_{10}$N(M) curve (black dots in Figure 3.2), and selecting the maximum value of this derivative. Then, the G-R parameters are determined by a linear fit of $\log_{10}$N(M) curve for magnitudes greater than the MOC. The results of this method are shown in Figure 3.2.

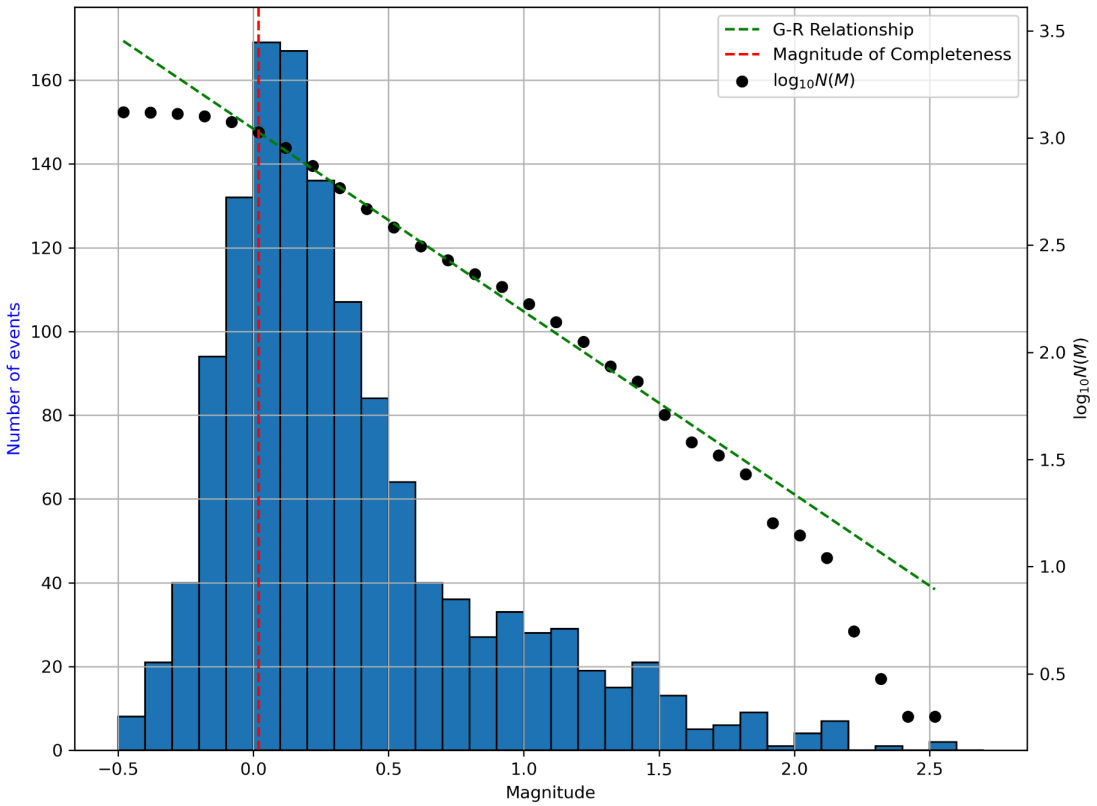

Figure 3.2: The frequency magnitude distribution of the catalog. The blue histogram represents the number of events within a 0.1 magnitude bin. The red dashed line represents the MOC, as determined by the MAXC method. The green dashed line shows the slope of the line corresponding to the a- and b-values estimated by the MAXC method. Black dots and the right Y-axis correspond to the logarithm of the number of events above a certain magnitude value.

The resulting MOC is 0.02, and the b-value is 0.85.

The second method that was used to calculate the b-value and MOC was the goodness of fit test (GFT) method of Wiemer & Wyss (2000). The GFT method models the G-R distribution for various values of a, b, and MOC. The parameters for the model with the best fit to the $\log_{10}$N(M) data are accepted as the solution. The results from using this method are much more consistent with expectation (Figure 3.3). The resulting MOC is 0.0, and the b-value is 0.9.

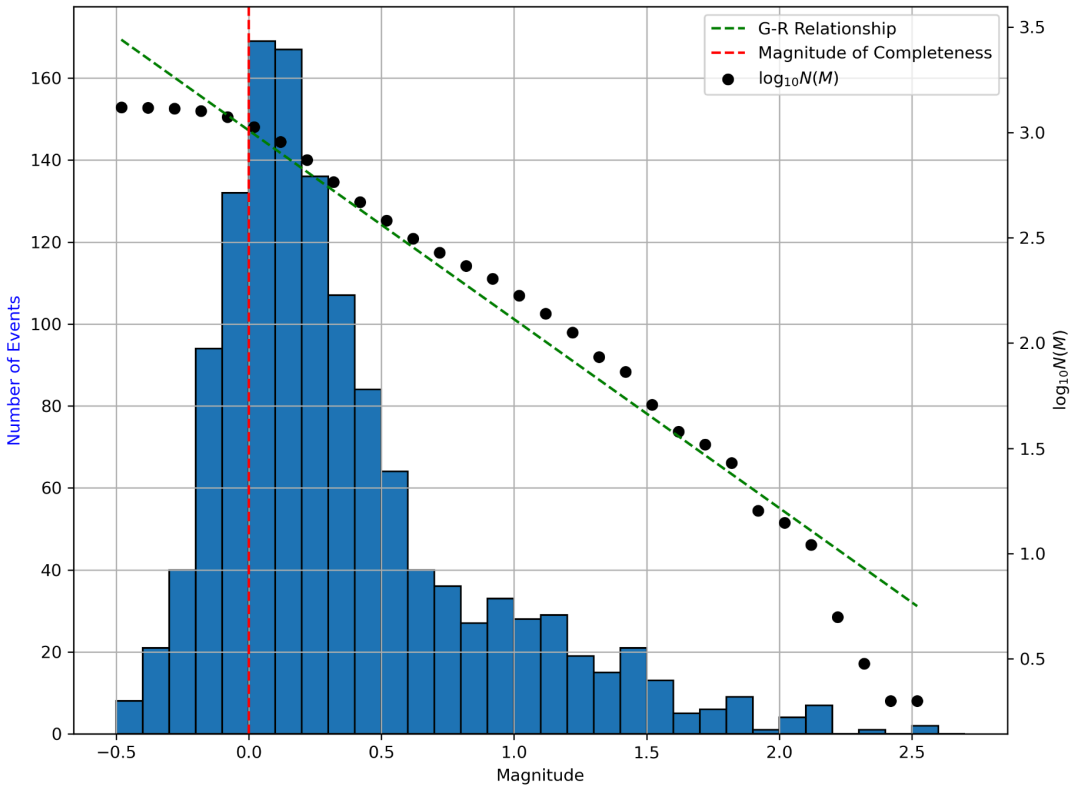

Figure 3.3: The frequency magnitude distribution of the catalog. The blue histogram represents the number of events within a 0.1 magnitude bin. The red dashed line represents the MOC, as determined by the GFT method. The green dashed line shows the slope of the line corresponding to the a- and b-values estimated by the MAXC method. Black dots and the right Y-axis correspond to the logarithm of the number of events above a certain magnitude value.

There are several clusters of seismicity, visible in map view in Figure 3.4. These clusters are all associated with industry activities in the area, and are primarily associated with HF operations rather than WD.

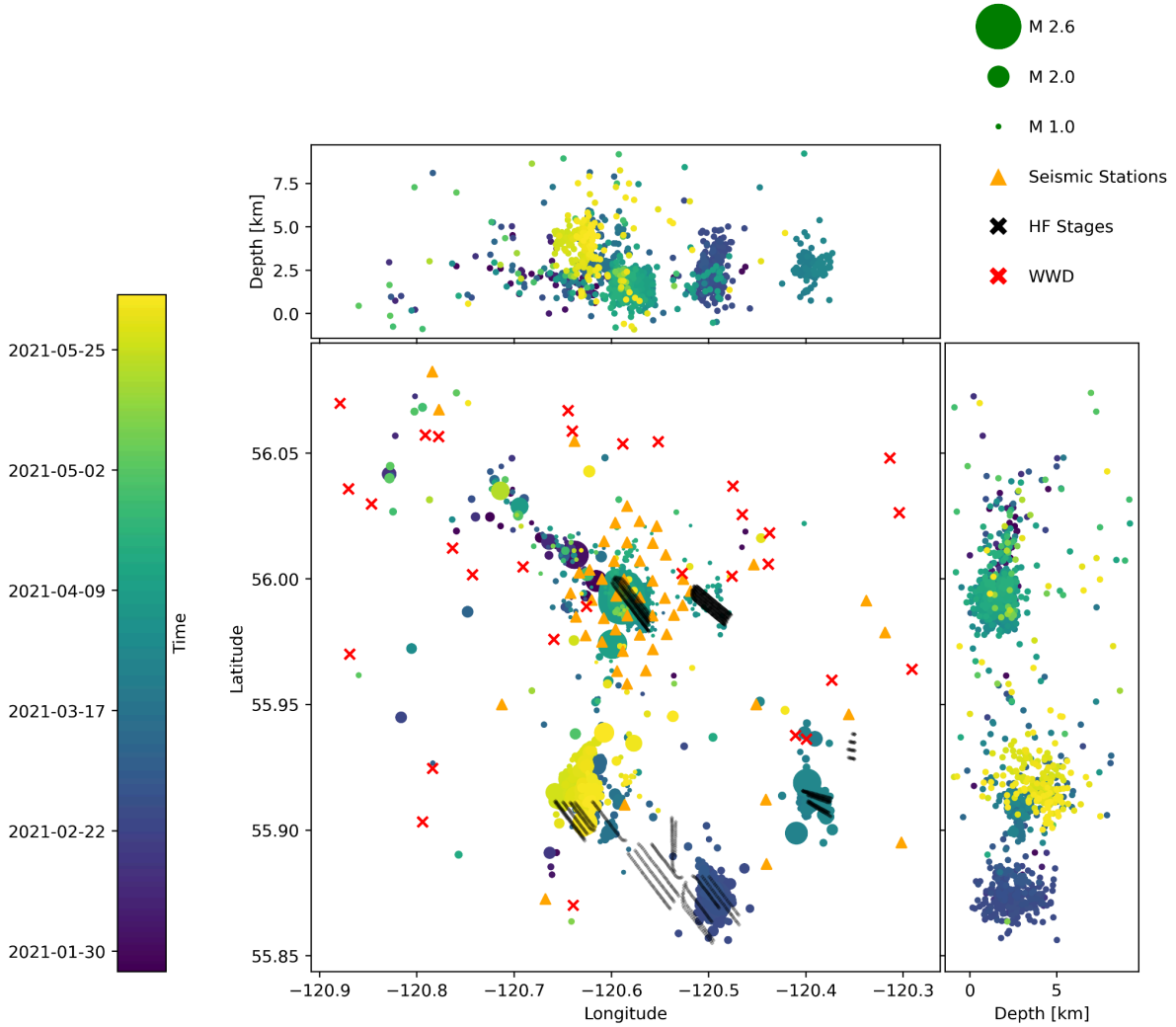

Figure 3.4: Map view and depth projections of relocated seismicity with industry activities plotted. All HF wells active from 2021-01-26 to 2021-06-05 are shown, and all WD wells from 1990-01-01 to 2021-05-06 are shown.

The mainshock in the catalog had a magnitude of M 2.6. This event was located only 161 m away from the nearest HF stage (Figure 3.5) and occurred during a time period when the Tower Lake HF operation was actively injecting fluids. Hence it is highly likely that the mainshock was triggered by the Tower Lake HF operation.

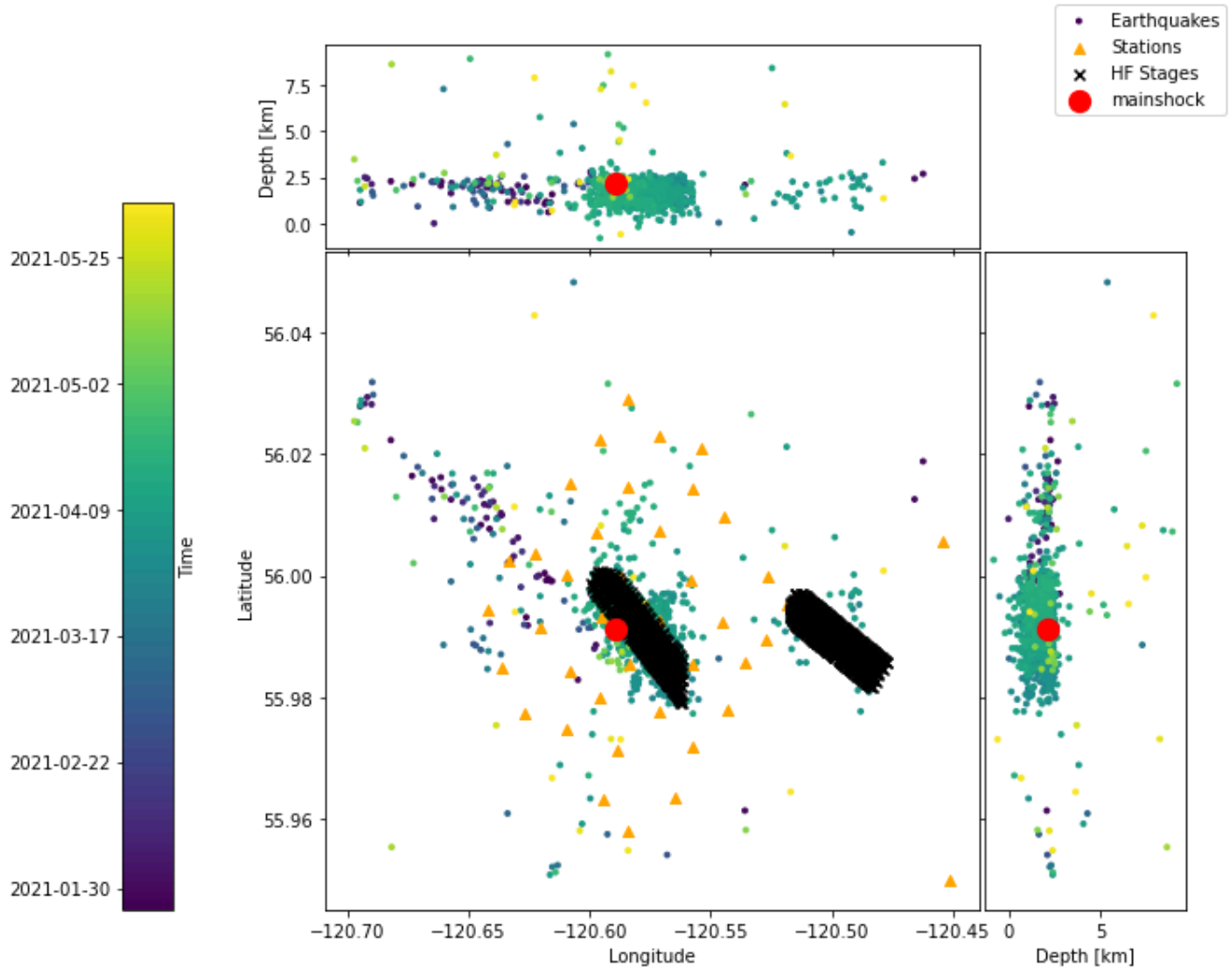

Figure 3.5: Magnified map view and depth projections of the mainshock.

The occurrence of the mainshock did not appear to affect the rate of seismicity in the following time period (Figure 3.6). This is likely due to the influence of the HF operations, which causes the seismicity following the mainshock pattern to deviate from the modified Omori decay curve of Utsu (1961). The modified Omori decay curve is a mathematical model that predicts the exponential decay of aftershock frequency with time after a large earthquake. Because the earthquake magnitudes do not follow the Omori law decay pattern, further analysis on this subject is not performed. The HF operations continued after the mainshock, which is likely why there is a higher rate of seismicity than predicted by the Omori decay curve.

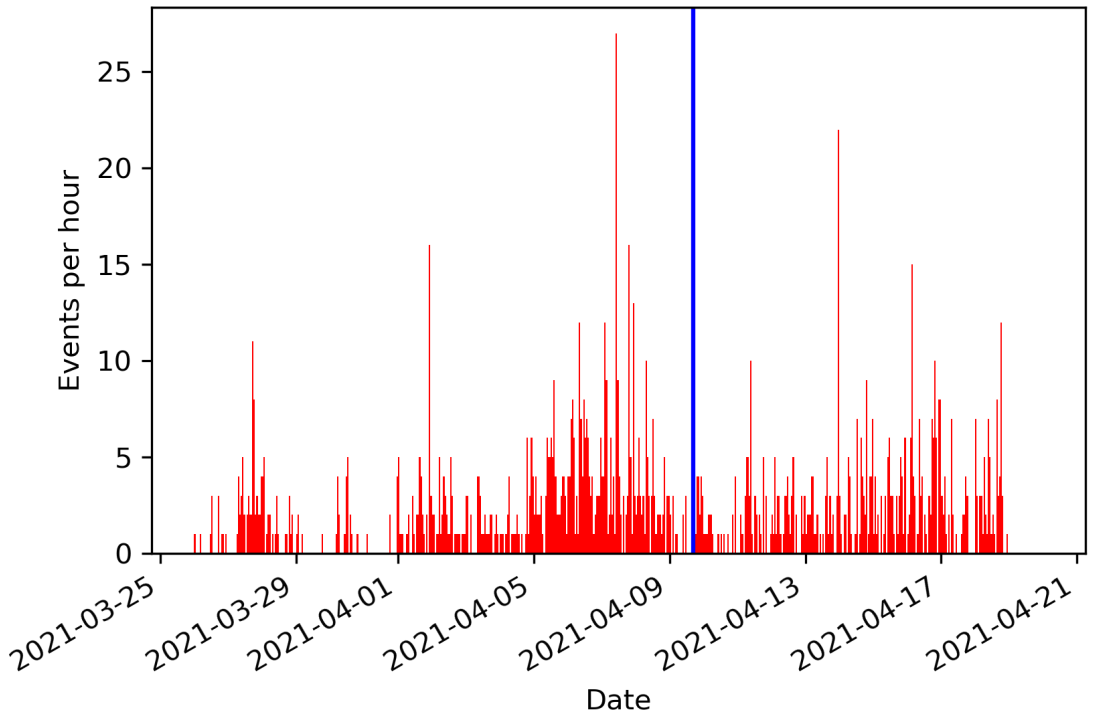

Figure 3.6: Frequency of earthquakes in the relocated earthquake catalog.The blue line denotes the occurrence time of the mainshock.

3.3 Tomography

Because the earthquake location problem (Section 3.2) depends on both the phase time measurements and seismic velocity model, the P-wave velocity model is inverted for in the joint earthquake relocation and tomography. This provides greater accuracy in the relocation, as well as providing information about the subsurface structure. In total 3,470,712 observations were used for the inversion, which is 93.4% of the original dataset. The main feature visible in the tomography results is a distinct low-velocity zone (LVZ). This LVZ occurs in very close proximity to the HF wells (Figure 3.7), which extend from approximately 0.5 km to 2.5 km in depth (Figure 3.8). Figure 3.7 also shows a high-velocity spike at 2.75 km depth in the northeast corner of the study area, and a low-velocity spike at 3.50 km depth in the west of the study area. Both of these spikes occur away from the center of the array,

and are likely artifacts resulting from the non-uniqueness of the velocity model solution recovered by tomographic inversion.

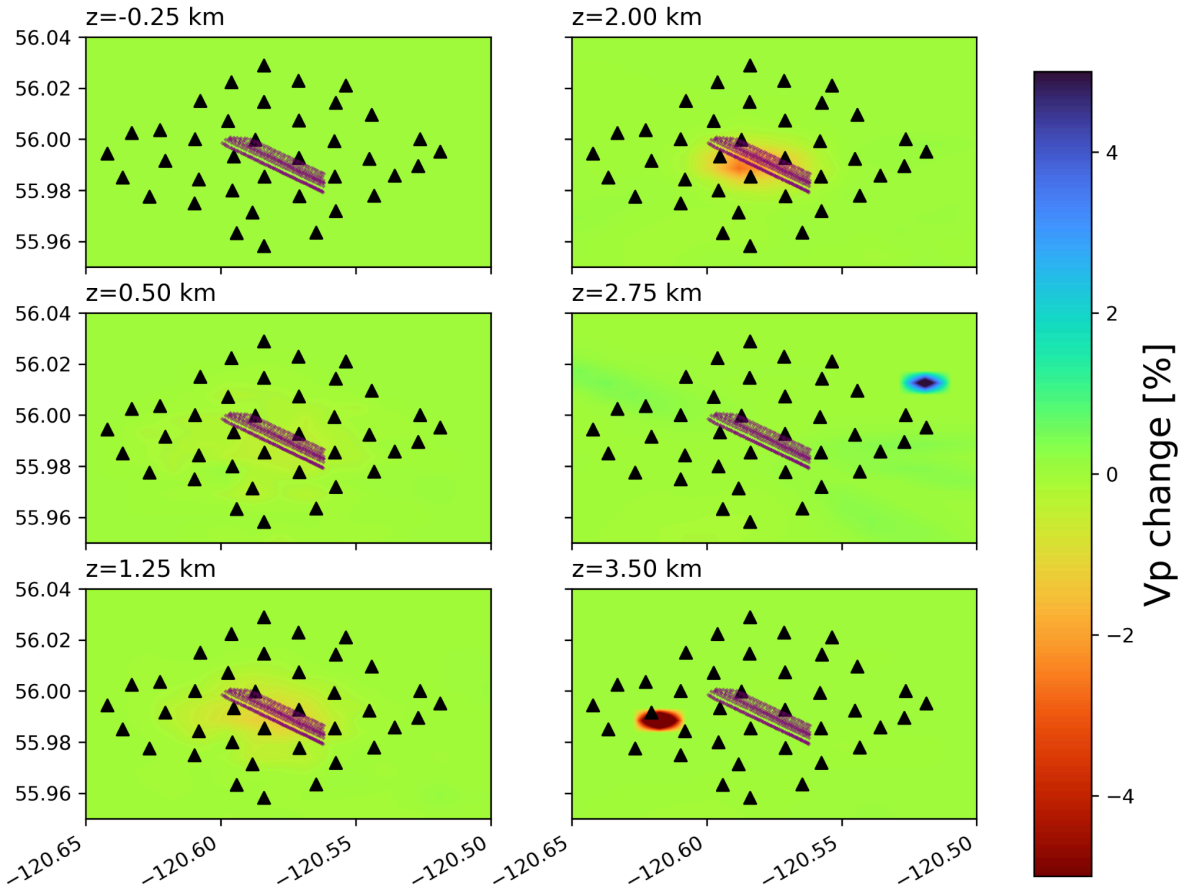

Figure 3.7: Depth cross-sections of the tomographic model. The velocity anomaly is represented as the percent change from the average velocity of each layer in the inverted model. Black triangles represent seismic stations. Purple lines represent HF wells.

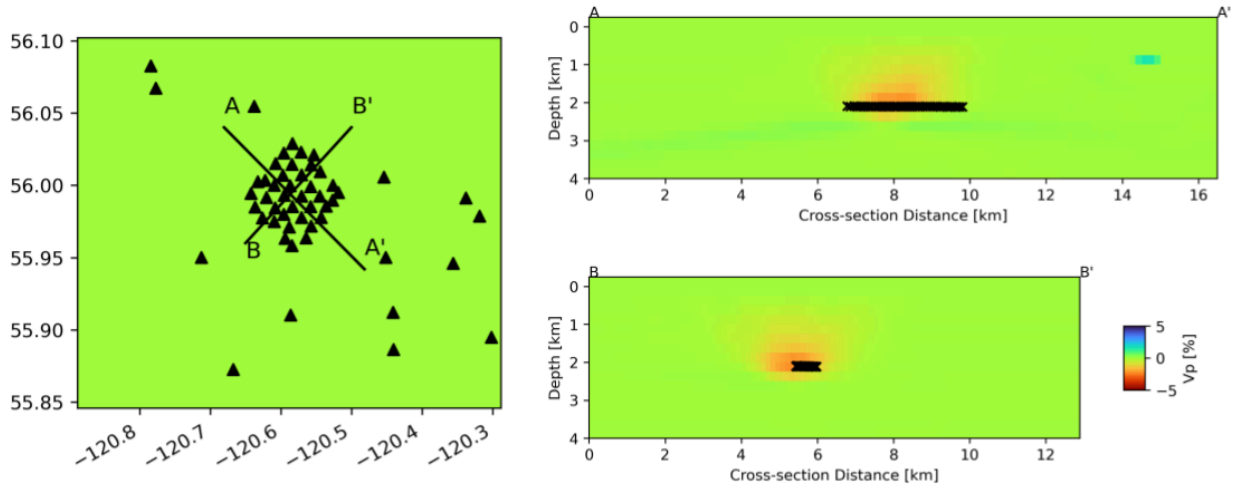

Figure 3.8: Map view and vertical cross-sections of the tomographic model. HF stages are plotted as black X's in the cross-section. Seismic stations are plotted as black triangles in the map view plot. The map view plot is included to show the cross-section traces with respect to the seismic networks.

In order to provide a qualitative estimate of the sensitivity of the model to subsurface velocity variations, the derivative weighted sum (DWS) values are plotted (Figure 3.9). The DWS is calculated for each grid node by taking the partial derivative of the earthquake phase travel times with respect to the model parameters (Equation 10 from Thurber and Eberhart-Phillips, 1999). The DWS is analogous to raypath density. Areas with a large DWS value are crossed by many raypaths, and are likely to be well resolved by the model. In Figure 3.9, the DWS value is large in the center of the seismic array, and corresponds to the apparent LVZ in Figures 3.7 and 3.8. The correlation between the large DWS values and the LVZ will be discussed in Section 4.4.

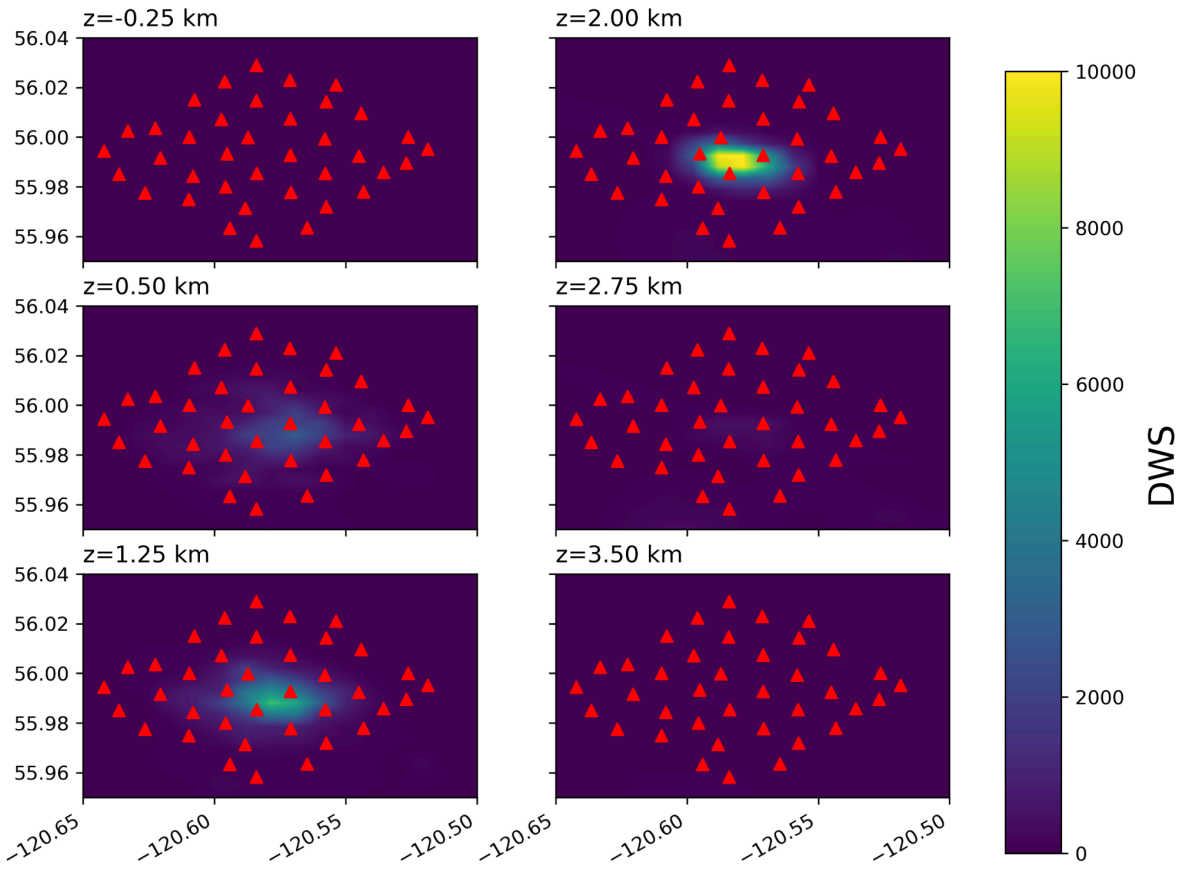

Figure 3.9: DWS values for horizontal slices of the tomographic model. The DWS is represented by color, and red triangles represent seismic stations.

3.4 Focal mechanisms

The results from Section 2.1.6 are presented in this section. All of the calculated focal mechanisms were for events in close proximity to the Tower Lake HF operations. Only the double couple components of the moment tensor were considered, in order to avoid over-interpreting any non-double couple components retrieved from this first motion polarity analysis.

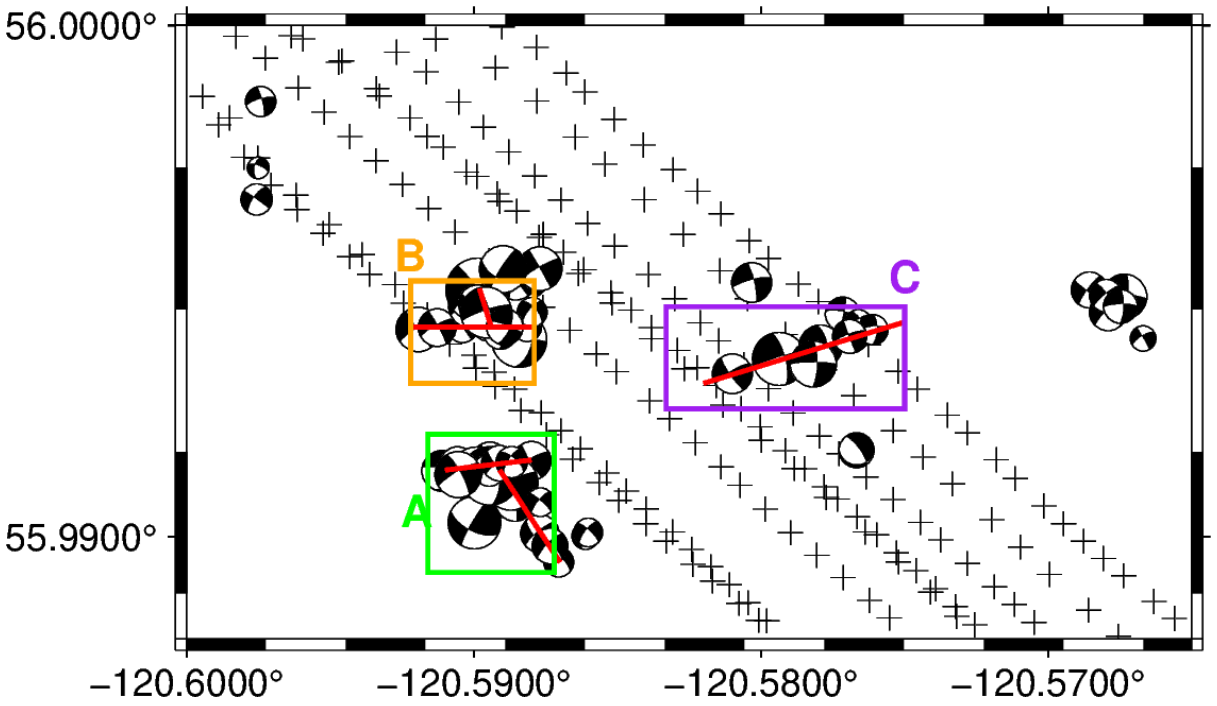

Figure 3.10: Focal mechanisms with lineations depicted. Three different lineations are depicted using a red line. Black crosses represent HF stage locations. The colored boxes represent areas that events were extracted from for Figure 3.14.

In this region, the azimuth of the maximum horizontal compressive stress direction (S_{Hmax}) is estimated to be 43.0° (Heidbach et al., 2018). The focal mechanisms are generally consistent with this stress field, as the compressional axes of the focal mechanisms tend to be aligned with the S_{Hmax} (Figure 3.10). The S_{Hmax} for the region fell within the compressive quadrant of all 78 focal mechanisms. All of the calculated focal mechanisms have a dominant strike-slip component, which is expected given the regional stress field.

A particular concern for HF operators is the possibility of previously unmapped faults that may be susceptible to triggering by HF operations. For example, the 2021 Luxian earthquake in the Sichuan Basin was an induced event that occurred along a previously unmapped fault (Zhao et al., 2023). Faults may be identified by microseismicity patterns, allowing HF operators to alter their operation plans, and avoid triggering the rupture of these faults.

In order to identify potential faults, a combination of the relocated earthquake catalog and focal mechanisms was used. Lineations in the relocated earthquake catalog indicate potential faults. If focal mechanisms can be calculated for several earthquakes in these lineations, further evidence of a fault may be available. When the possible fault planes of the earthquakes align, this is further evidence that the lineation may be caused by microseismicity occurring along a fault plane. This is especially true if the focal mechanisms are consistent with the regional stress field.

There are three clusters that are readily apparent in Figure 3.10. These clusters contain five lineations. These lineations all meet three criteria. The first criterion is that at least five earthquakes must be included in the lineation, The second criterion is that the focal planes from at least three of the calculated focal mechanisms must be within 30° of the strike of the lineation. The final criterion is that the sense of fault slip that the lineation suggests must be consistent with the local stress field. A magnified view of each of the clusters is provided in Figures 3.11, 3.12, and 3.13.

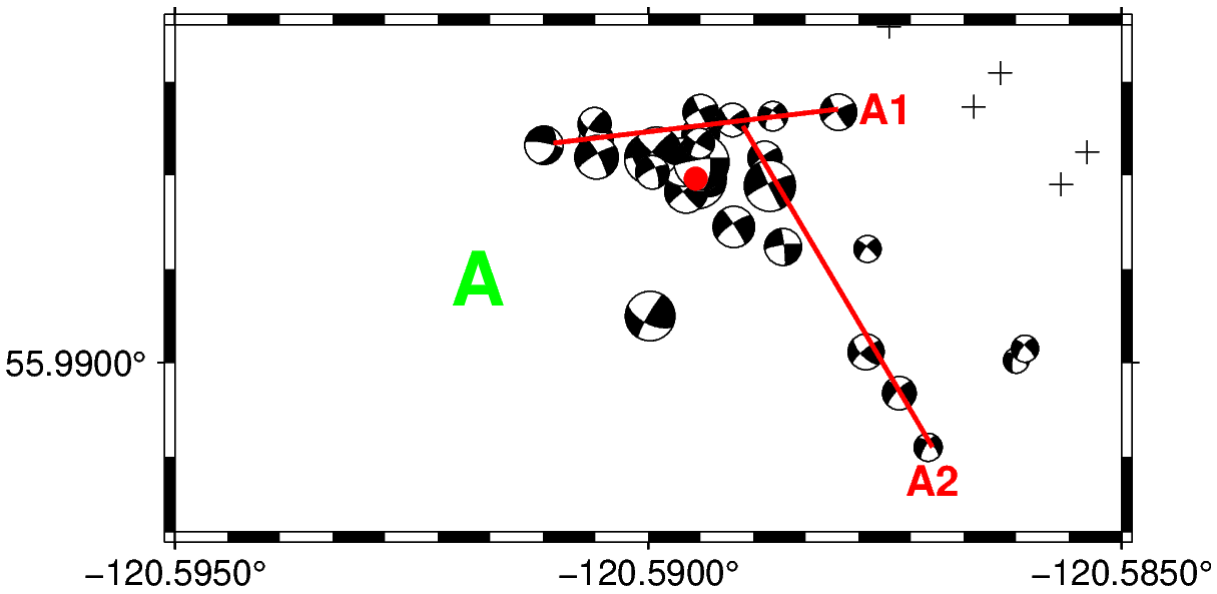

Figure 3.11: Cluster A from Figure 3.10 in greater detail. The mainshock location is depicted as a red dot. The lineations are labeled A1 and A2.

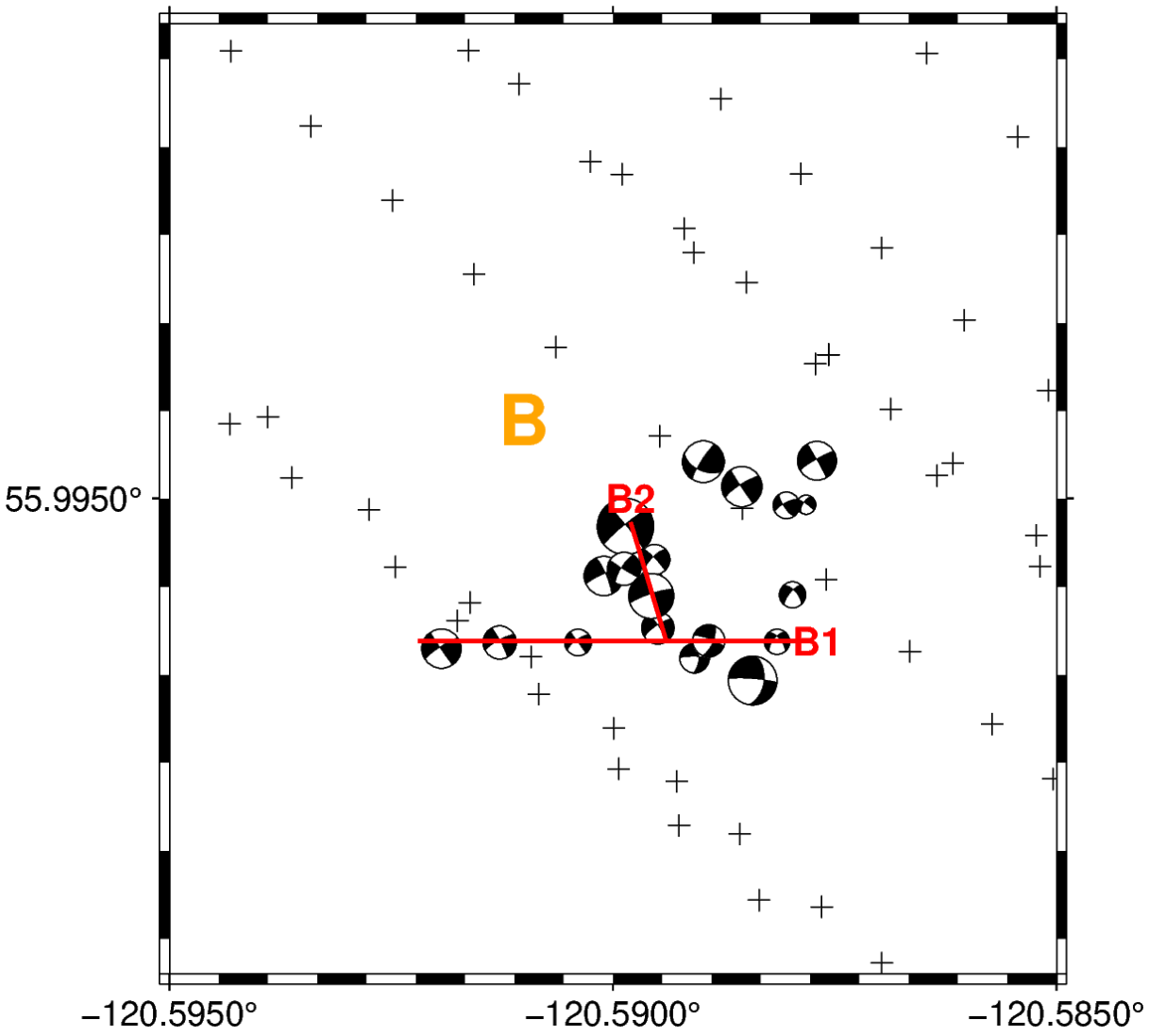

Figure 3.12: Cluster B from Figure 3.10 in greater detail.

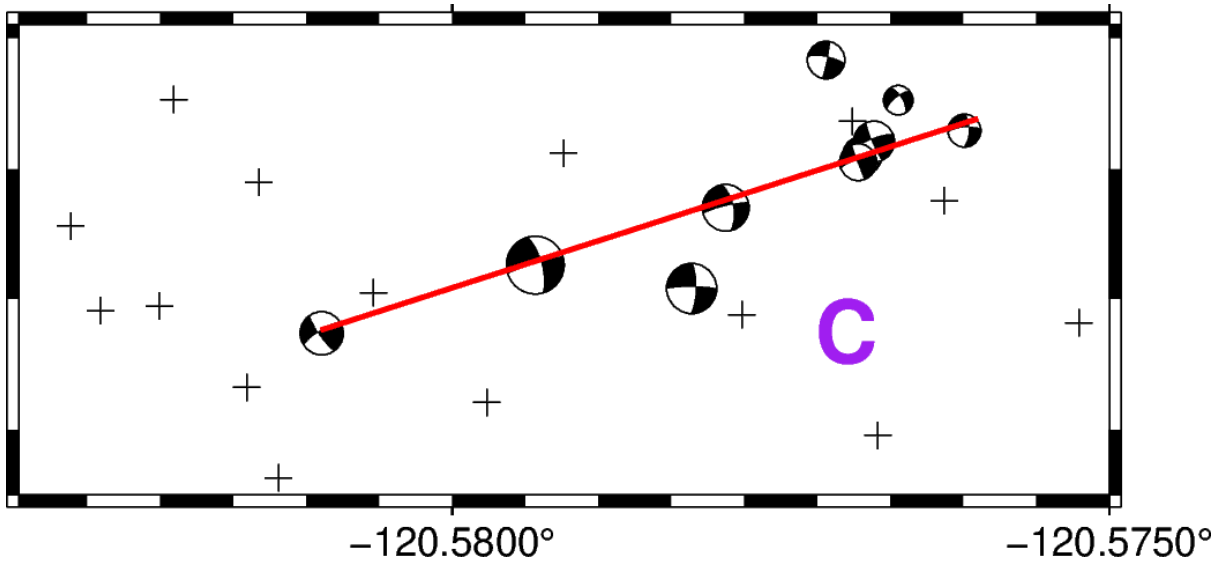

Figure 3.13: Cluster C from Figure 3.10 in greater detail.

Figure 3.14 shows the time evolution of events in each cluster. In cluster A from Figure 3.11, several events occurred on these lineations preceding the M 2.6 mainshock. A similar pattern also appears in cluster B from Figure 3.12, which includes the second largest event in the catalog, at M 2.5. A different pattern occurs for cluster C from Figure 3.13, with the largest event in the cluster occurring before most of the seismicity in this area. A gap in seismicity is observed in Figure 3.14. This is likely due to a pause in HF operations. There is a slight lag time in the decrease in seismic activity, compared to the pause in injection operations. This is likely because the pore pressure remains elevated for a short period of time, before the pore pressure increase has become so dispersed that earthquakes can no longer be triggered.

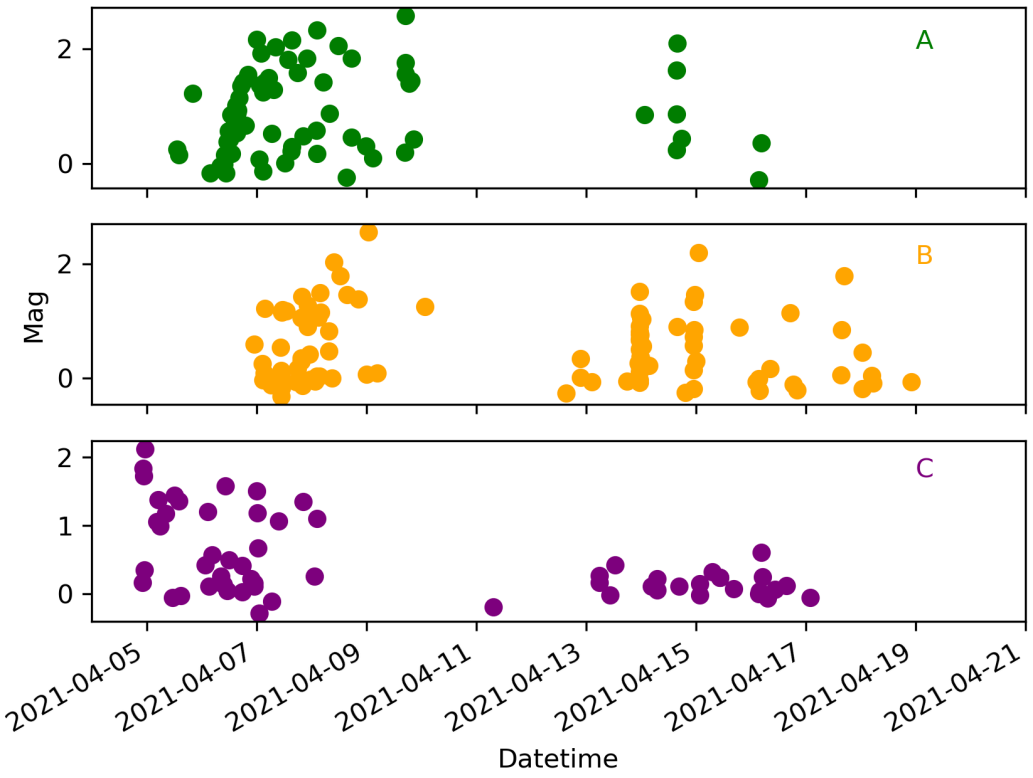

Figure 3.14: The evolution of seismicity with time in each of the clusters from Figure 3.10. Colors correspond to the area in Figure 3.10 that events in this figure were extracted from.

Assuming the lineations are strike-slip faults, the expected magnitude for a full rupture was calculated for each fault using the circular crack model (Eshelby, 1957). The seismic moment of a circular crack rupture is given by:

$$M_0 = \frac{16}{7}\Delta\sigma \cdot r^3 \quad (5)$$

where $\Delta\sigma$ is the stress drop, and r is the radius of the circular crack. In order to estimate the moment magnitude from the seismic moment, the equation of Hanks and Kanamori (1979) was used.

$$M_w = \frac{2}{3} log_{10}\left(M_0\right) - 10.7 \quad (6)$$

where M_w is the moment magnitude, and M_0 is the seismic moment in dyne · cm. In Equation 5, the stress drop is an unknown parameter. Magnitudes of potential earthquakes along the lineations are estimated using two assumed values of stress drop: a large value of 10 MPa and a small value of 1 MPa. This provides an upper and lower bound on the estimated magnitudes.

Table 3.1: Estimated magnitudes for each lineation, with both large and small stress drops.

Lineation	Stress Drop (MPa)	Estimated Magnitude	Lineation Length (m)
A1	1	2.4	250
A1	10	3.1	250
A2	1	2.4	245
A2	10	3.0	245
B1	1	2.5	267
B1	10	3.1	267
B2	1	1.5	87
B2	10	2.1	87
C	1	2.9	455
C	10	3.6	455

Due to the dense seismic station pattern, and good azimuthal coverage, the focal mechanisms are generally well constrained. In Figure 3.15, the focal mechanism with the lowest standard deviation in strike is displayed. This focal mechanism has a high number of observations compared to the other focal mechanisms. This explains why the standard deviation in strike is so low, as the model is well constrained by the observations. Figure 3.16 shows the focal mechanism with the highest standard deviation in strike. The focal mechanism for this event is poorly constrained.

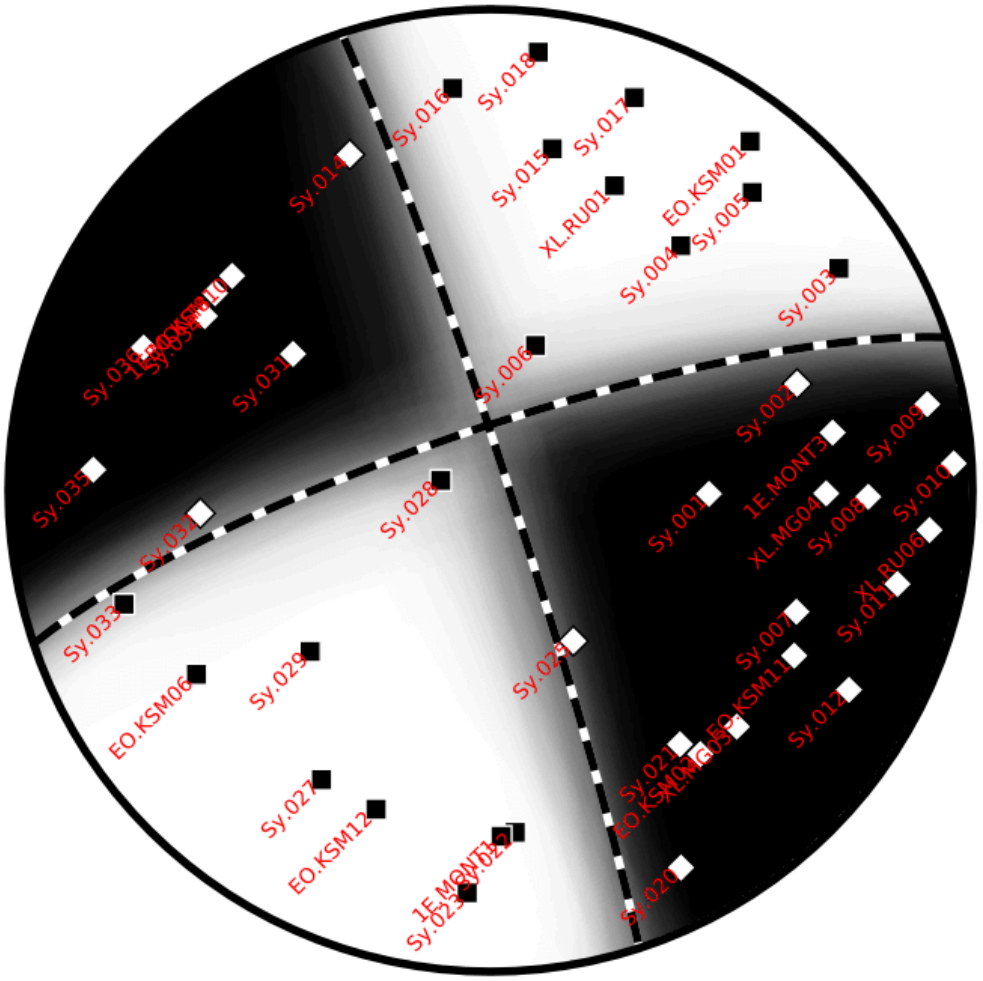

Figure 3.15: A high quality focal mechanism.

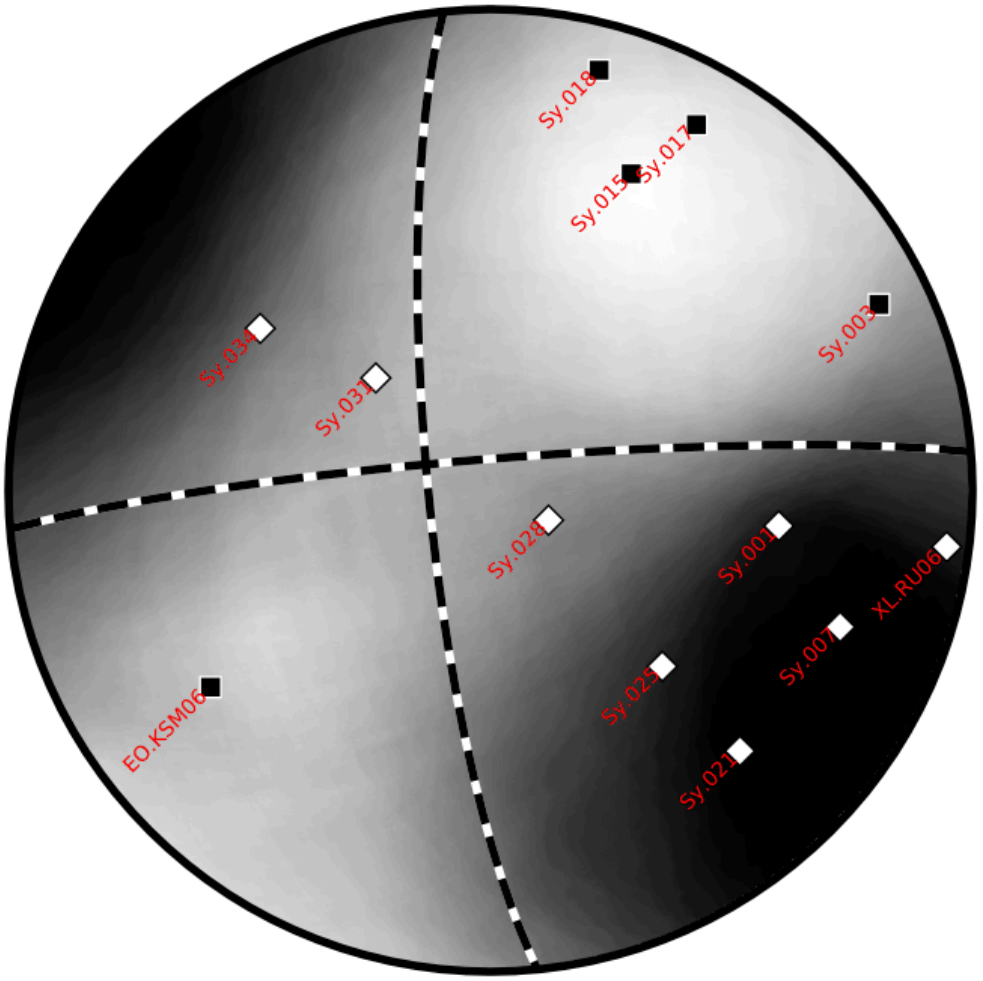

Figure 3.16: A low quality focal mechanism.

3.5 Comparison of Seismicity with Injection

Several injection parameters were made available to use. These parameters include injection pressure, rate and volume. These parameters were sampled once per second. In order to calculate the cumulative injected fluid volume for each well, the injection rate was integrated over time. Based on cumulative injected fluid volume, there are two distinct phases among all the wells. The transition between phases occurred on 2021-04-09. The injection rate displayed similar patterns between each of the phases (Figure 3.17).

Throughout each phase, injection rates increased. The maximum injection rates of each phase were similar.

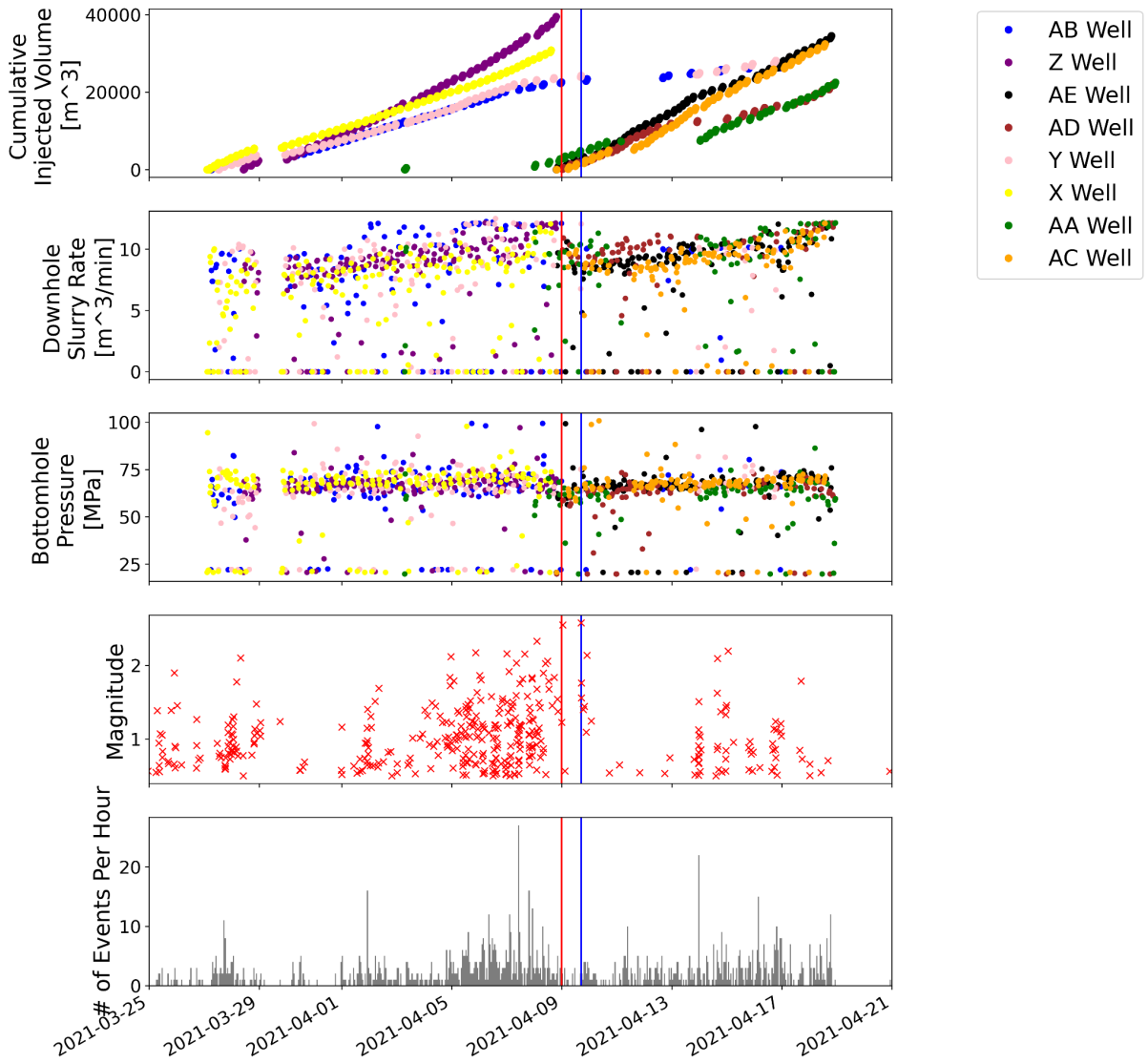

Figure 3.17: Injection parameters over time for all wells in the Tower Lake HF operation. Slurry is the combination of all HF fluids. Seismicity is also plotted as red x's. The red line denotes the change between the first and second phases of the HF operation. The blue line denotes the time of the mainshock.

The highest hourly rate of seismicity occurred during the first phase of operations. The largest magnitude event occurred during the beginning of the second phase. The injection pressures varied throughout the operation, with no obvious trends. Maximum pressures in both phases were similar (Figure 3.17).

The cumulative injected volume (Figure 3.17) is significantly different from the injected pressure and injection rate. The wells in the first phase of operations have slightly higher injection volumes than wells in the second phase of operations.

It is interesting to note that as the cumulative injected fluid volume increases during the first phase of operations, the seismic activity also increases. This is consistent with the McGarr (2014) interpretation of seismicity triggered by injected fluids, where the cumulative moment release (ΣM_0) is linearly related to injected volume as:

$$\Sigma M_0 = \frac{2\mu(3\lambda+2G)}{3}\Delta V \qquad (7)$$

where μ is the coefficient of friction, λ is Lamé's first parameter, G is the modulus of rigidity, and ΔV is the change in subsurface volume due to injected fluids. In order to estimate the moment release expected for a given volume, some assumptions must be made. Following the methodology of McGarr (2014), we assume that $G = 3 \times 10^{10}$ Pa, $\lambda = G$, and $\mu = 0.6$. We also used the b-value of 1.4 determined by the GFT method. Using these values, the expected moment release is equivalent to a magnitude 3.9 earthquake. This is significantly larger than the largest detected event of M 2.6. The cumulative seismic moment released by all the earthquakes in the catalog is equivalent to a magnitude 3.2 earthquake. This value is still lower than the value predicted by the McGarr relationship. This is expected, as the McGarr relationship represents an upper bound to the released seismic moment.

It is also interesting to note that the rate of seismicity increases with injected volume (Figure 3.17). This is consistent with the observations made by Schultz et al. (2018) in the Duvernay play. The Schultz et al. (2018) study considered multiple HF well pads targeting the Duvernay play, creating a robust link between injected volume of HF operations and the rate of seismic activity. Our study investigates a single HF well pad targeting the Montney

formation. Despite the difference in study areas, these two studies suggest that the physical mechanism of HF-induced earthquakes may be similar.

3.6 Earthquake Migration Patterns

The migration of earthquakes through space and time can provide valuable information on subsurface fluid dynamics, as well as the induced earthquake triggering mechanism. Specifically, earthquake migration patterns can identify any events that may not have been triggered by pore pressure diffusion, as pore pressure diffusion is limited by the diffusivity of the subsurface. In order to analyze the earthquake migration pattern, the earthquake catalog was separated into two sections. The first section was composed of events that occurred before 2021-04-08, while the second section was composed of events that occurred after 2021-04-10, corresponding to the two main phases of injection operations. The first event in each section was assumed to be the diffusion initiation point. The time difference and distance from this point was calculated for all earthquakes in each section. Each section was broken into four-hour time windows, and the 95th percentile of distance was calculated for each window. Following the methodology of Shapiro et al. (1997), the maximum diffusion front distance is estimated as:

$$r = \sqrt{4\pi D t} \tag{8}$$

where r is the distance away from the initiation point, D is the diffusivity, and t is the elapsed time after the fluid flow initiation. Following the method of Yu et al. (2019), the diffusivity was estimated by performing a non-linear least squares fit between the 95th percentile distances and Equation 8, with diffusivity as a free parameter. For the first section of earthquakes, the diffusivity was estimated to be 0.86 m^2/s, while for the second section it was estimated to be 1.08 m^2/s. Most events fall within these theoretical diffusion fronts, although there are events that exceed the theoretical diffusion front (Figures 3.18 and 3.19). In order to compare the

measured diffusivity to other possible values of crustal diffusivity, theoretical diffusion fronts are also shown on Figure 3.18. A large value of 10 m^2/s was used to estimate a fast diffusion front, as this is one of the larger diffusivities observed for the earth's crust by Scholz (2002). A low value of 0.2 m^2/s was selected, as this was the value observed by Yu et al. (2019). In addition, diffusivity values were calculated using a curve fit to the 100th percentile of the distances, and the 90th percent of the distances. For the first section of earthquakes, the diffusivity calculated using the 100th percentile of distances was 1.3 m^2/s, and the diffusivity calculated using the 90th percentile of earthquakes was 0.7 m^2/s. For the second section of earthquakes, the diffusivity calculated using the 100th percentile of distances was also 1.3 m^2/s, and the diffusivity calculated using the 90th percentile of earthquakes was 1.0 m^2/s.

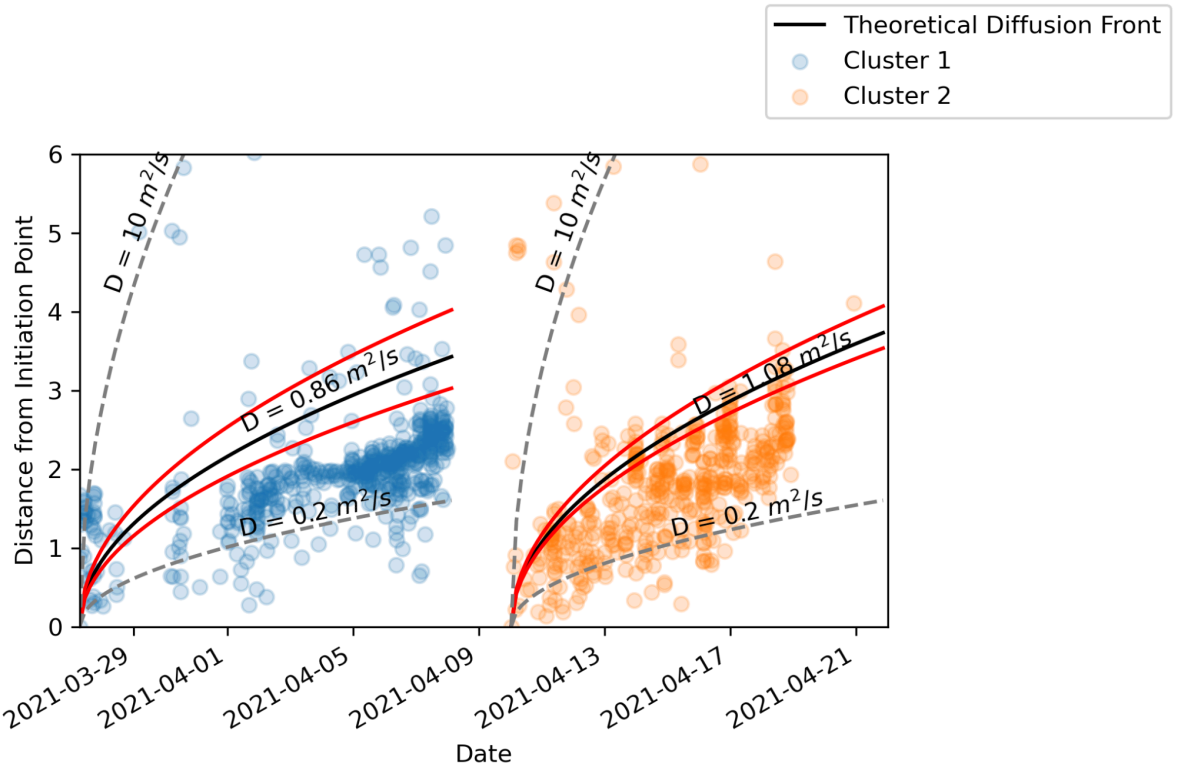

Figure 3.18: Seismicity migration of the Tower Lake earthquake catalog. The first section of earthquakes is colored in blue, while the second section is colored in orange. Theoretical diffusion fronts for each section are also plotted. The gray dashed lines show calculated diffusion fronts for an extremely high diffusivity of 10 m^2/s and a more typical value of 0.2 m^2/s. The black dashed lines show the calculated diffusion fronts for the estimated diffusivity values for the Tower Lake earthquake catalog. The red lines show a diffusivity curve fit to the 100th percentile of the distances, and the 90th percentile of the distances.

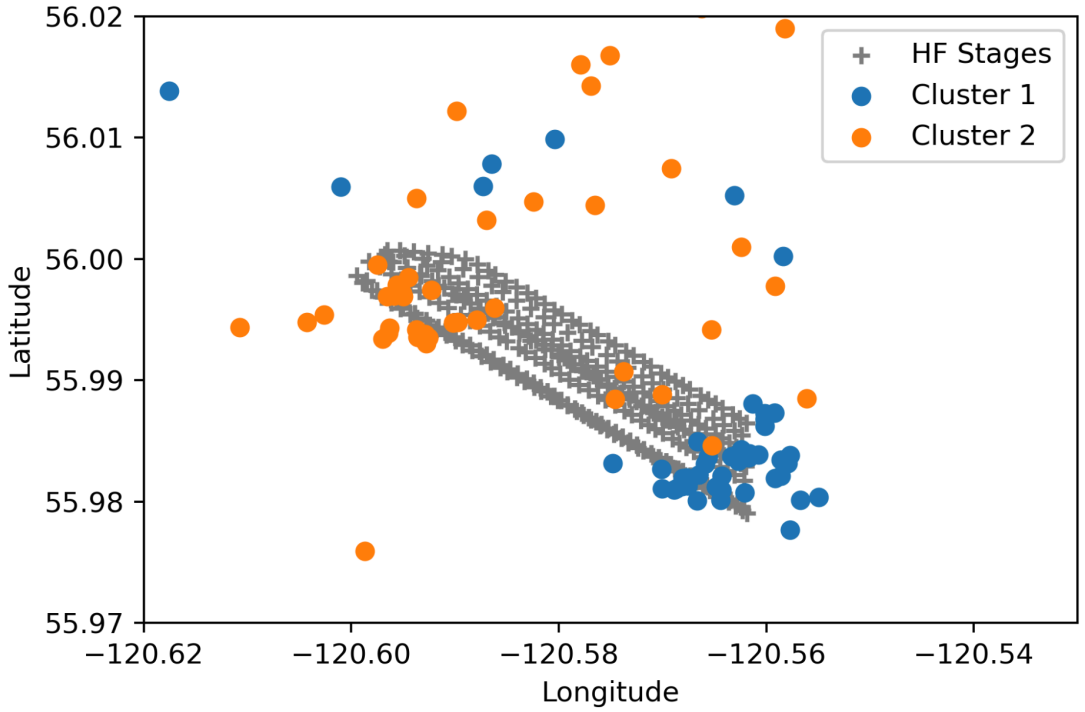

Figure 3.19: Events that occurred before the theoretical diffusion front reached their location. The colors correspond to clusters identified in Figure 3.18.

4. Discussion

4.1 Seismicity Clusters

As shown in Figure 4.1, there are several large scale clusters of seismicity in the earthquake catalog. Investigating these clusters can provide valuable information about the triggering mechanisms of the seismicity, as well as potential seismogenic structures. Each of these clusters correlates with a specific industry operation in both space and time. The main Tower Lake operation has a large seismicity cluster in close proximity, which is almost certainly due to the injection operations. All of these clusters appear to correlate with HF operations, rather than WD operations. This is expected for the WCSB, as WD generally has a lower likelihood to trigger IIE in this area (Atkinson et al., 2016).

The calculated diffusivity values of 0.86 m^2/s and 1.08 m^2/s are relatively high compared to the value of 0.2 m^2/s observed by Yu et al. (2019). One possible hypothesis for this disparity is that there are several high permeability pathways in the area of the Tower Lake HF operations. The faults identified through analyzing earthquake locations and focal mechanisms could possibly function as a high permeability pathway, causing an increase in the observed diffusivity.

In our study, the spatial extent of the seismicity was similar to the spatial extent of the HF wells. Because the injection point of the well changes with each HF stage, the assumption of a fixed point source injecting fluids into the subsurface may not be valid. In some cases, the change in location of each stage could possibly exceed the distance that could have been reached by the pore pressure diffusion front. This would have the effect of artificially inflating our diffusivity estimates. However, it is likely that the actual value of diffusivity in the Tower Lake area is higher than Yu et al.'s (2019) value of 0.2 m^2/s, as almost every event occurs

before the theoretical arrival of pore pressure increase predicted by a diffusivity of 0.2 m^2/s (Figure 3.18).

Several events also occur before the pore pressure diffusion is expected to reach their location, even with the large values of diffusivity observed (Figure 3.18). Two distinct behaviors are observed in events that occur outside of the theoretical diffusion front (Figure 3.19). The first behavior is observed in Cluster 1. These events occur near the toe of the HF well. It is likely that these events were triggered by the poroelastic effect, rather than pore pressure increase. No other wells were active in the area before the events in Cluster 1 occurred, so it is not possible that these events were triggered by pore pressure increase from another well. The events in Cluster 1 also occur well before the pore pressure increase is expected to arrive at their location. Even with an extremely large diffusivity value of 10 m^2/s, several events in Cluster 1 occur before the estimated increase in pore fluid pressure (Figure 4.1). A possible explanation for these events is that they were triggered by the poroelastic effect.

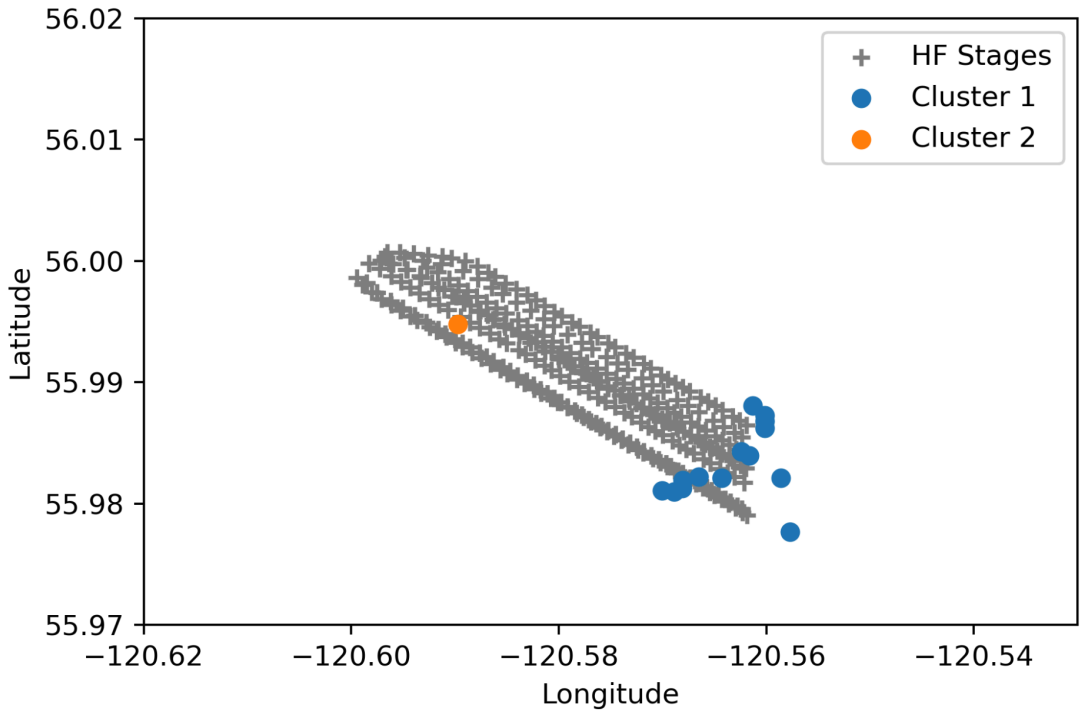

Figure 4.1: Events that occur before the estimated pore pressure increase, calculated using a diffusivity of 10 m^2/s.

The second behavior is observed in Cluster 2. These events occur near the heel of the HF well. It is likely that these events are triggered by the pore pressure increase from the first phase of injection, but due to the pore pressure diffusion delay they occurred during the second phase of HF operations.

4.2 Spatial Lineations of Seismicity

Several lineations appear in the map view of the relocated seismicity catalog (Figure 3.10). These lineations, along with the focal mechanism dataset, strongly suggest the presence of crustal faults. Knowledge of crustal faults can provide information on seismic hazards, as well as earthquake behavior and triggering mechanisms.

There are five distinct lineations in Figure 3.10. Magnitudes were calculated for a theoretical strike-slip earthquake rupturing the entire length of the lineation. In clusters A and B, the estimated magnitudes ranged from M 1.5 to M 3.1, depending on the length of the lineation and the stress drop. The larger estimated magnitudes are quite close to the observed magnitudes of the largest event in each cluster, which are M 2.6 for Cluster A, and M 2.5 for Cluster B. This suggests that the M 2.6 and M 2.5 events ruptured a significant portion of each lineation, if not the entire lineation. Clusters A and B also displayed two sets of lineations each, suggesting a conjugate fault system. If these lineations are faults, both pairs of lineations would be consistent with the local stress field.

The lineation in Cluster C is much longer than the lineations observed in Clusters A and B, with an estimated magnitude varying from M 2.9 to 3.6. The largest observed event in Cluster C was M 2.1, which is significantly smaller than the predicted size if the entire lineation had ruptured. Based on this information, there may be faults near the Tower Lake HF operation that could host an M 3 or greater earthquake, if a sufficient stress perturbation

is applied. Such an earthquake has the potential to cause damage to the infrastructure nearby, and would likely be felt by residents in the immediate neighborhood (British Columbia Oil and Gas Commission, 2012) .

The rate of earthquakes through time on each lineation presents an interesting pattern. In Clusters A and B, many smaller earthquakes occur along the lineation before the largest event in each cluster occurs. This precursory seismic activity indicates that several earthquakes along the lineation were triggered by the pore pressure increase from the HF operation. These earthquakes illuminate the fault structure in the area, and in this case provide information about the location and magnitude of the largest earthquake in the sequence. However, Cluster C does not exhibit this behavior. The largest earthquake occurs near the beginning of the sequence, and is followed by smaller events. No precursory activity is observed for this sequence. Given these examples, no reliable indicator of future earthquakes can be identified. However, if lineations of earthquakes are observed for other HF operations, this may be a sign that a fault is being re-activated by the HF operations, and that a larger earthquake might be possible, such as in the cases of Clusters A and B, Figure 3.14. This does not mean that future earthquakes can be predicted based on the faults being illuminated by seismicity. However, a fault being illuminated by seismicity is a potential warning sign that a larger event may occur in the future.

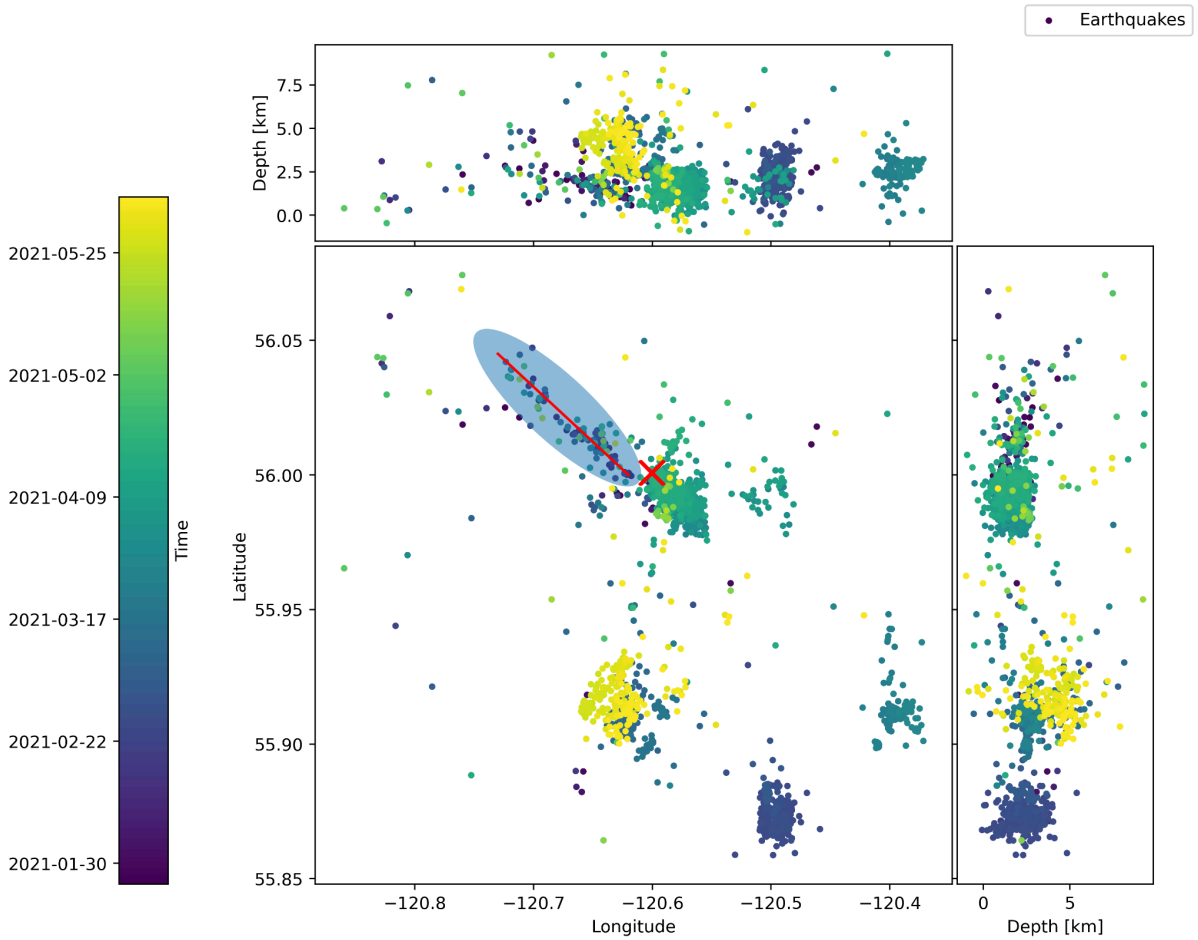

Figure 4.2: Seismicity, with the NW to SE lineament highlighted in red. The Tower Lake well head is depicted by the red X symbol.

There is also a large-scale NW to SE lineament visible to the NW of the Tower Lake HF operation (Figure 4.2). The seismicity along this lineament could be caused by fluid transport, with the fault acting as a high permeability conduit. However, all the seismicity along the lineament occurred before the start of the Tower Lake operations. Therefore the seismicity cannot be associated with the Tower Lake well. If this lineament is a fault, it would be well oriented for a large thrust event. However, this lineament is not well suited to host a strike-slip event. Using the same method as in Section 3.4, we estimated the potential magnitude if the lineament ruptured. The length of the lineament is 8.5 km. For this length, and a stress drop of 1 MPa, the estimated magnitude is M 5.5. For a stress drop of 10 MPa, the estimated magnitude is M 6.1. While we cannot confirm if this structure is a fault, the potential seismic risk from this feature may be significant. Unfortunately, none of the

earthquakes in this lineament had enough phase measurements to compute an accurate focal mechanism. Several significant induced thrust events have occurred in the WCSB, such as the 2018 M4.5 Fort St. John earthquake (Salvage and Eaton, 2022), and the 2022 M5.6 Peace River earthquake (Schultz et al., 2023).

4.3 Correlation of Injection with Seismicity

It is difficult to delineate which injection parameter had the greatest effect on seismicity. The Tower Lake HF operation was characterized by two phases of injection activity. The first phase had a higher cumulative volume, pressure, and injection rate compared to the second phase. The first phase was associated with a greater earthquake rate. In addition, the injection wells of the different phases are separated spatially. Generally, wells in the first phase are located to the SW of wells in the second phase. In a zoomed-in plot of seismicity (Figure 4.3), several dense clusters appear near the wells of the first phase. This suggests that there may be some structural features in this area that are particularly sensitive to triggering from injection operations of the first phase.

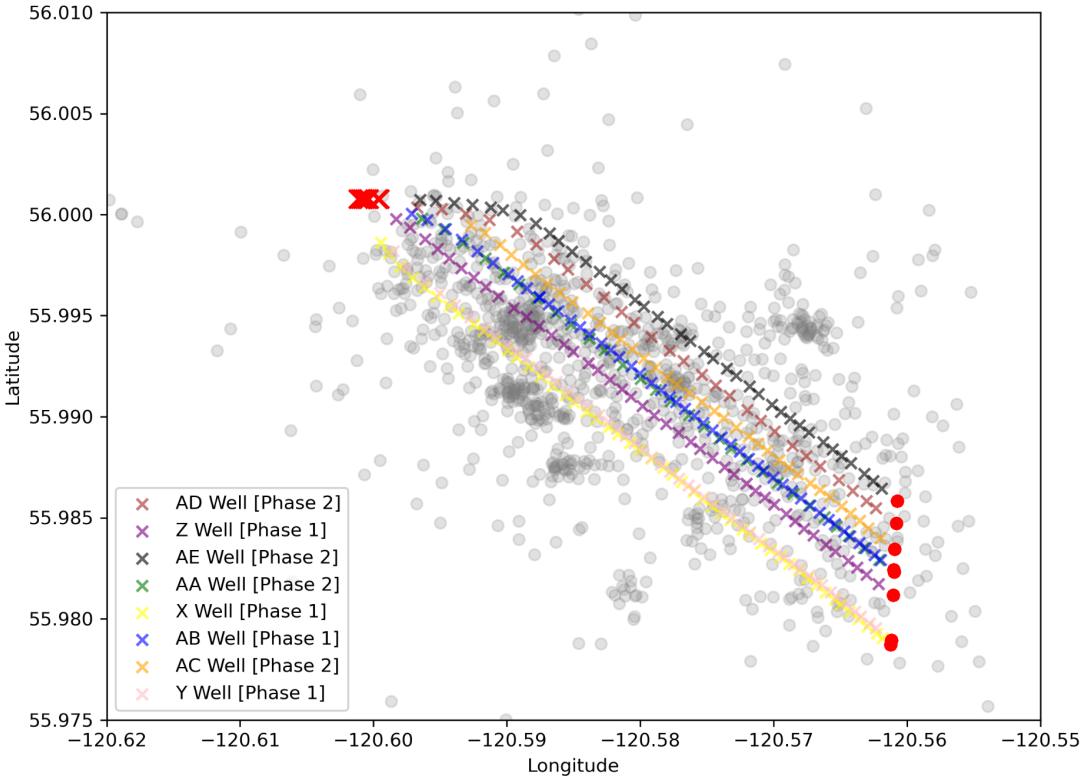

Figure 4.3: Magnified view of seismicity and HF stage locations. The different colors represent the different wells of the Tower Lake HF pad. Red circles represent the toe of the well, and red X's represent the borehole locations of each well. Seismicity is represented by gray dots. All HF stage locations from the Tower Lake operation are plotted.

It has been well established by McGarr (1976, 2014) that the cumulative seismic moment is linearly related to injected volume in the subsurface. The constant of proportionality of this line is dependent on Lamé's elastic parameters, as well as the coefficient of friction, as given in Equation 7. The cumulative seismic moment is dependent on two factors: the number of earthquakes and their magnitudes. When injection is initiated, both the rate of seismogenesis and the magnitude of earthquakes may increase to accommodate the change in volume in the subsurface. In the Tower Lake earthquake catalog, the largest magnitude event accounted for roughly 12% of the cumulative seismic moment. The largest 10 events accounted for approximately 50% of the cumulative seismic moment. In the nearby Duvernay formation, another study clearly observed an increase in seismicity rate due to an increase in HF injection volume (Schultz et al., 2018). Our results, as well as

Schultz et al. (2018), provide evidence that the McGarr relationship is applicable to HF scenarios in the WCSB.

The injection pressure shows some correlation with increased seismicity; however, it is not possible to separate the effect of injection pressure from other variables, as injection rate and cumulative injected fluid volume are correlated. A previous study by Wang et al. (2022) investigated the effects of different HF operational parameters, and found that the maximum and average treatment pressure did not have a significant correlation with either the rate or magnitude of induced seismicity. However, Wang et al. (2022) did find that the breakdown pressure, which is the pressure at which the target formation begins to fracture, had some correlation with induced seismicity. Wang et al. (2022) also found that the instantaneous shut-in pressure, which is the pressure at which fractures close after the HF operation, was correlated with induced seismicity. Breakdown pressure and instantaneous shut-in pressure can only be measured once per injection stage. Because of this fact, we did not investigate the breakdown pressure or instantaneous shut-in pressure, as the number of injection stages in this study was limited. In order to truly delineate the effects of injection pressure, further research is needed, ideally with an experiment that isolates changes in pressure.

Another parameter that was investigated was the target formation depth. Amini et al. (2022) found that the target formation had some influence on the likelihood of triggering induced seismicity, with the Middle Montney having a higher percentage of wells that triggered earthquakes. The Tower Lake operation targeted all three of the Upper, Middle, and Lower Montney. In both phases of the HF operations there are wells targeting all three sub-formations concurrently (Figure 4.4), and so no dependence on target formation can be identified.

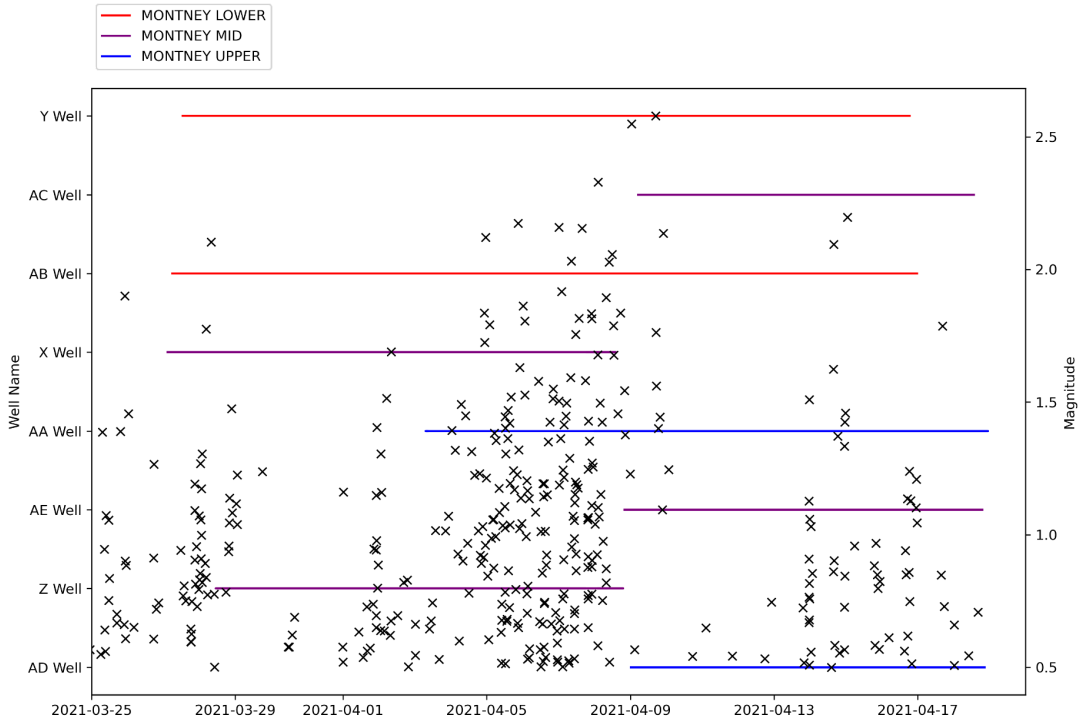

Figure 4.4: Seismicity and well target formations.

4.4 Seismic Imaging of HF Operation

There is one prominent LVZ in close proximity to the Tower Lake HF operation in the tomographic image (Figures 3.7, 3.8). There are several possible interpretations of this LVZ.

Because many of the earthquakes in the Tower Lake earthquake catalog are located close to the HF wells, the area around the HF wells has the greatest ray path density. Very few raypaths intersect with cells outside of the injection area, as shown in Figure 3.8. This suggests that the inversion is not sensitive to the subsurface anywhere outside of the area of injection operations. Because of this lack of sensitivity, the LVZ surrounding the Tower Lake HF operation may well be an artifact. A likely explanation for the LVZ is that the actual subsurface velocities are somewhat lower than the input model, and the actual subsurface velocities are represented in the LVZ, while the rest of the estimated model is only slightly changed from the input model. In order to test this hypothesis, a synthetic test was performed. A synthetic velocity model was derived from the initial model used for the original

inversion, with 10% lower velocities. Then, synthetic double difference travel time measurements were calculated using the synthetic velocity model, with the same sources and receivers as the original inversion. Then, an inversion was performed using these synthetic measurements, using the same parameters and initial velocity model as the original inversion. The results of this test are shown in Figure 4.5. The tomographic results of the synthetic inversion are very similar to the tomographic results of the original inversion. This suggests that the LVZ observed in the original tomographic model is likely an artifact.

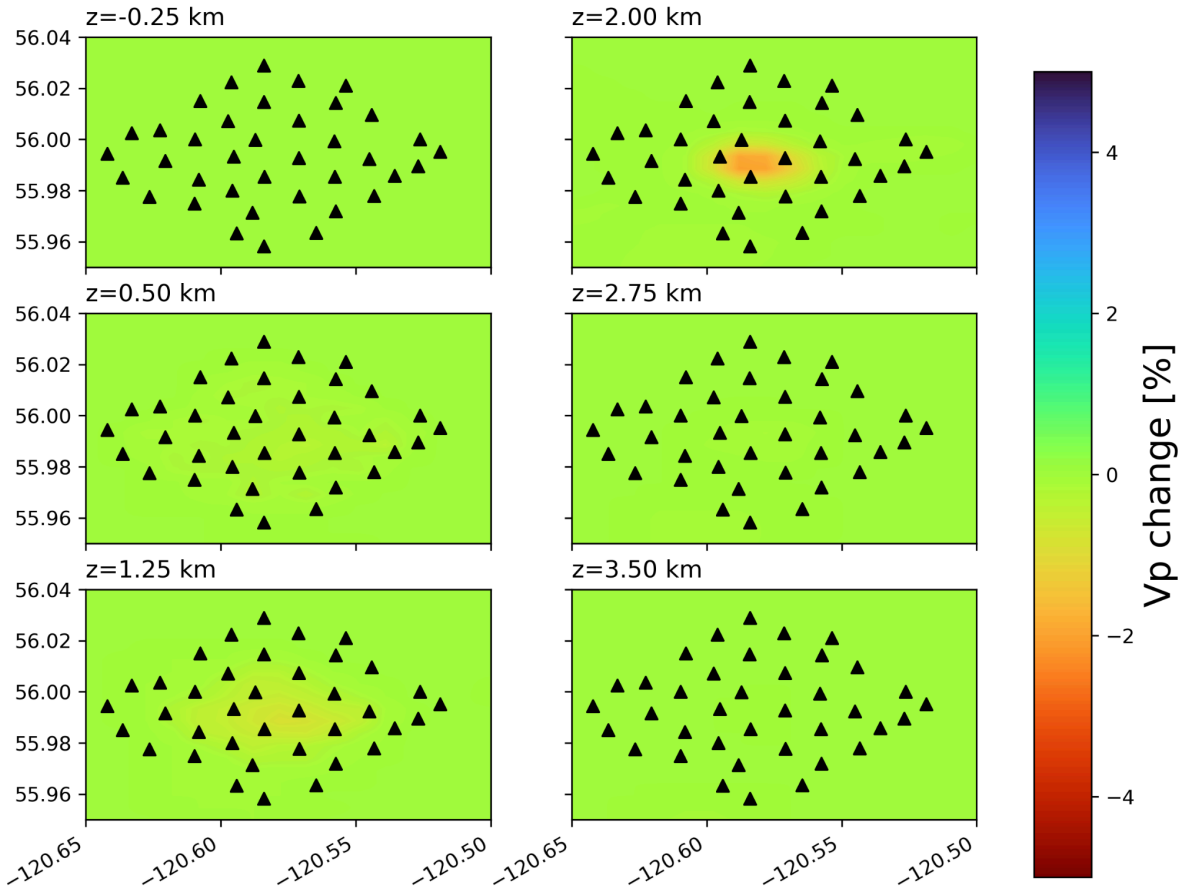

Figure 4.5: Tomography results of the synthetic inversion. The velocity anomaly is represented as the percent change from the average velocity of each layer in the inverted model. Black triangles represent seismic stations. The HF wells are omitted for clarity.

Body wave tomography will always be limited by the number and location of earthquake sources in the dataset. In many cases, the seismicity caused by subsurface injection will be clustered around the injection operations. This means that the raypath density near the

injection operations will be relatively high, while raypath density in areas away from the injection operation will be low. This may be a distinct disadvantage if features away from the main injection operation are of interest. This disadvantage also hinders the comparison of features that are near the injection site with features that are far from the injection site. Other methods, such as the ambient noise tomography that does not depend on earthquake sources, may be much better suited to monitoring the change of seismic properties associated with injection operations.

5. Conclusions

In this thesis, a HF operation near Tower Lake, BC, was studied using the techniques of observational seismology. An earthquake catalog was produced, double difference earthquake relocation and tomography were performed, focal mechanisms were calculated, and injection information was analyzed for correlations with seismicity. Seismic and injection data with an unprecedented level of resolution were made available for this project.

The earthquake catalog was produced using state of the art machine learning techniques. The resulting catalog included 3377 events that passed our quality control criteria. While there were observed to be some false detections in the earthquake catalog, these were easily removed.

In order to analyze earthquake patterns, a high-resolution earthquake relocation was performed using the TomoDD software. Of the 3377 earthquakes in the original catalog, 2193 earthquakes were successfully relocated. The MOC of the relocated catalog was estimated to be 0.8, using the GFT technique. The b-value was found to be 1.4, which is higher than most global seismic catalogs, but consistent with other induced seismicity earthquake catalogs. The largest earthquake in the catalog was M 2.6. One main cluster of earthquakes was identified and associated with the Tower Lake HF operation. However, many other clusters of seismicity were also detected and associated with other HF operations in the area. The migration patterns of the induced seismicity were investigated. A large value for diffusivity was required to explain the rate of earthquake migration, suggesting that the subsurface in the Tower Lake area is highly fractured.

A tomographic inversion was also performed. A 3-D velocity model was extracted that covered all of the seismic stations, and extended to 4 km depth. A prominent LVZ was observed in the vicinity of the HF wells, but it is likely that this LVZ is an artifact caused by

the lack of resolution in the tomographic model. Ambient noise tomography may be more suitable for monitoring subsurface injection, as the resolution is not dependent on earthquakes being triggered by the injection operation.

Focal mechanisms were also manually calculated for this dataset. In total, 78 focal mechanisms were calculated. Due to the good azimuthal coverage of the seismic stations, the focal mechanisms were well constrained. The focal mechanisms were predominantly strike-slip, and all were consistent with the S_{Hmax} in the area. Several clear lineations were visible in the earthquake catalog. Using these lineations and the focal mechanism dataset, some small-scale faults were identified. Estimates for the magnitude of potential earthquakes on these faults were made. In Clusters A and B, the faults were at least partially ruptured by induced events. The lineation in Cluster C could potentially host an M3.0 or larger earthquake. Clusters A and B produced several small-scale earthquakes before larger events occurred on the lineations.

The high-resolution injection dataset provided an unique opportunity to investigate the correlation between injection parameters and seismicity. It was found that injection pressure and injection rate had a minimal effect on seismicity, while the cumulative volume was highly correlated with seismic activity. This is generally consistent with the McGarr hypothesis, with the McGarr relationship bounding above all the events in the earthquake catalog.

This study provided several developments to the understanding of induced seismicity. One particularly important observation was the detection of several foreshocks along identified faults. In this case, the foreshocks provided information about the following mainshocks from each fault. Characterizing faults and monitoring seismic activity during injection operations could allow oil and gas operators to preemptively modify their operations to avoid triggering larger seismic events. Evidence for a highly-fractured target formation was also observed. The diffusivity estimated in this study ranged from 0.86 m^2/s to 1.05 m^2/s. This is significantly

higher than typically observed in tight shale formations. Our findings also support the observations of Yu et al. (2019), which suggested that the Montney formation is highly fractured. A high diffusivity value allows for earthquakes to be triggered by pore pressure diffusion further away, and much sooner than expected for mediums with a more typical diffusivity value. We also found that most of the earthquakes in the Tower Lake catalog were likely triggered by pore pressure diffusion, rather than the poroelastic effect. This corroborates the findings of several other studies suggesting that pore pressure diffusion is the most likely triggering mechanism for induced seismicity in the Montney formation. This is also consistent with analysis of the injection information, as the cumulative injected fluid volume was linearly related to the amount of seismic moment released.

6. References

Amini, A., Eberhardt, E., Rogers, S., Venables, S., & Gaucher, M. (2022). Empirical and numerical investigation into the influence of fluid injection volume and rate on induced seismicity in the Montney Formation, northeastern British Columbia. *Journal of Petroleum Science and Engineering*, *213*, 110423.

Atkinson, G. M., Eaton, D. W., Ghofrani, H., Walker, D., Cheadle, B., Schultz, R., ... & Kao, H. (2016). Hydraulic fracturing and seismicity in the Western Canada Sedimentary Basin. *Seismological Research Letters*, *87*(3), 631-647.

British Columbia Energy Regulator. (2020). Retrieved 2024-04-29. *Regulator Partnering with Tower Lake Residents for Seismic Testing (NR 2020-02).* https://www.bc-er.ca/news/commission-partnering-with-tower-lake-residents-for-seismic-testing/

British Columbia Oil and Gas Commission. (2012). Retrieved 2024-08-18. *Investigation of Observed Seismicity in the Horn River Basin.* https://www.bc-er.ca/files/reports/Seismicity-and-Fracturing/investigation20of20observed20seismicity20in20the20horn20river20basinaug202012.pdf

Beyreuther, M., Barsch, R., Krischer, L., Megies, T., Behr, Y., & Wassermann, J. (2010). ObsPy: A Python toolbox for seismology. *Seismological Research Letters*, *81*(3), 530-533.

Biot, M. A. (1941). General theory of three‐dimensional consolidation. *Journal of Applied Physics*, *12*(2), 155-164.

Christensen, N. I. (1984). Pore pressure and oceanic crustal seismic structure. *Geophysical Journal International*, *79*(2), 411-423.

Dou, Z., Gao, T., Zhao, Z., Li, J., Yang, Q., & Shang, D. (2020). The role of water lubrication in critical state fault slip. *Engineering Geology*, *271*, 105606.

Eaton, D. W., & Schultz, R. (2018). Increased likelihood of induced seismicity in highly overpressured shale formations. *Geophysical Journal International*, *214*(1), 751-757.

Enlighten Geoscience Ltd. (2021). Pressure, Stress and Fault Slip Risk Mapping in the Kiskatinaw Seismic Monitoring and Mitigation Area, British Columbia. (ER-Seismic-2020-01) BC Oil and Gas Research and Innovation Society. https://www.bcogris.ca/files/projects/pre/er-seismic-2020-01-final-report-enlighten-ver-3.pdf

Eshelby, J. D. (1957). The determination of the elastic field of an ellipsoidal inclusion, and related problems. *Proceedings of the royal society of London. Series A. Mathematical and physical sciences*, *241*(1226), 376-396.

Farahbod, A. M., Kao, H., Cassidy, J. F., & Walker, D. (2015). How did hydraulic-fracturing operations in the Horn River Basin change seismicity patterns in northeastern British Columbia, Canada?. *The Leading Edge*, *34*(6), 658-663.

Font, Y., Kao, H., Lallemand, S., Liu, C. S., & Chiao, L. Y. (2004). Hypocentre determination offshore of eastern Taiwan using the Maximum Intersection method. *Geophysical Journal International*, *158*(2), 655-675.

Hanks, T. C., & Kanamori, H. (1979). A moment magnitude scale. *Journal of Geophysical Research: Solid Earth*, *84*(B5), 2348-2350.

Heidbach, O., Rajabi, M., Cui, X., Fuchs, K., Müller, B., Reinecker, J., ... & Zoback, M. (2018). The World Stress Map database release 2016: Crustal stress pattern across scales. *Tectonophysics*, *744*, 484-498.

Heimann, S., Kriegerowski, M., Isken, M., Cesca, S., Daout, S., Grigoli, F., ... & Dahm, T. (2017). Pyrocko-An open-source seismology toolbox and library.

Horner, R. B., Barclay, J. E., & MacRae, J. M. (1994). Earthquakes and hydrocarbon production in the Fort St. John area of northeastern British Columbia. *Can. J. Explor. Geophys*, *30*(1), 39-50.

Hubbert, M., & Rubey, W. W. (1959). Role of fluid pressure in mechanics of overthrust faulting: I. Mechanics of fluid-filled porous solids and its application to overthrust faulting. *Geological Society of America Bulletin*, *70*(2), 115-166.

Li, B. Q., Khoshmanesh, M., & Avouac, J. P. (2021). Surface deformation and seismicity induced by poroelastic stress at the Raft River geothermal field, Idaho, USA. *Geophysical Research Letters*, *48*(18), e2021GL095108.

Lomax, A., Virieux, J., Volant, P., & Berge-Thierry, C. (2000). Probabilistic earthquake location in 3D and layered models: Introduction of a Metropolis-Gibbs method and comparison with linear locations. *Advances in Seismic Event Location*, 101-134.

Lomax, A., & Curtis, A. (2001). Fast, probabilistic earthquake location in 3D models using oct-tree importance sampling. In *Geophys. Res. Abstr* (Vol. 3, No. 955, pp. 10-1007).

Mahani, A. B., & Kao, H. (2018). Local magnitude scale for earthquakes in the Western Canada Sedimentary Basin, northeastern British Columbia and northwestern Alberta. *Geoscience BC Summary of Activities*, 47-54.

Babaie Mahani, A. (2021). Seismic b value within the Montney play of northeastern British Columbia, Canada. *Canadian Journal of Earth Sciences*, *58*(8), 720-730.

Mahani, A. B., Malytskyy, D., Visser, R., Hayes, M., Gaucher, M., & Kao, H. (2021). Well-log-based velocity and density models for the Montney unconventional resource play in northeast British Columbia, Canada, applicable to induced seismicity monitoring and research. *Seismological Research Letters*, *92*(2A), 886-894.

McGarr, A. (1976). Seismic moments and volume changes. *Journal of Geophysical Research*, *81*(8), 1487-1494.

McGarr, A. (2014). Maximum magnitude earthquakes induced by fluid injection. *Journal of Geophysical Research: Solid Earth*, *119*(2), 1008-1019.

Pita-Sllim, O., Chamberlain, C. J., Townend, J., & Warren-Smith, E. (2023). Parametric testing of EQTransformer's performance against a high-quality, manually picked catalog for reliable and accurate seismic phase picking. *The Seismic Record*, *3*(4), 332-341.

Ojo, A. O., Kao, H., Visser, R., & Goerzen, C. (2022). Spatiotemporal changes in seismic velocity associated with hydraulic fracturing-induced earthquakes near Fox Creek, Alberta, Canada. *Journal of Petroleum Science and Engineering*, *208*, 109390.

Porter, J. W., Price, R. A., & McCrossan, R. G. (1982). The western Canada sedimentary basin. *Philosophical Transactions of the Royal Society of London. Series A, Mathematical and Physical Sciences*, *305*(1489), 169-192.

Price, R.A. (1994): Cordilleran Tectonics and the Evolution of the Western Canada Sedimentary Basin, G.D. Mossop and I. Shetsen (comp.), Canadian Society of Petroleum Geologists and Alberta Research Council, URL https://ags.aer.ca/atlas-the-western-canada-sedimentary-basin/chapter-2-cordilleran-tectonics , [Last accessed Feb 14, 2024].

Raleigh, C. B., Healy, J. H., & Bredehoeft, J. D. (1976). An experiment in earthquake control at Rangely, Colorado. *Science*, *191*(4233), 1230-1237.

Salvage, R. O., & Eaton, D. W. (2022). The influence of a transitional stress regime on the source characteristics of induced seismicity and fault activation: Evidence from the 30 November 2018 Fort St. John ML 4.5 induced earthquake sequence. *Bulletin of the Seismological Society of America*, *112*(3), 1336-1355.

Scholz, C. H. (2002). The Mechanics of Earthquakes and Faulting. *The Mechanics of Earthquakes and Faulting*, 496.

Schultz, R., Atkinson, G., Eaton, D. W., Gu, Y. J., & Kao, H. (2018). Hydraulic fracturing volume is associated with induced earthquake productivity in the Duvernay play. *Science*, *359*(6373), 304-308.

Schultz, R., Woo, J. U., Pepin, K., Ellsworth, W. L., Zebkar, H., Segall, P., ... & Samsonov, S. (2023). Disposal from in situ bitumen recovery induced the ML 5.6 Peace River earthquake. *Geophysical Research Letters*, *50*(6), e2023GL102940.

Shapiro, S. A., Huenges, E., & Borm, G. (1997). Estimating the crust permeability from fluid-injection-induced seismic emission at the KTB site. *Geophysical Journal International*, *131*(2), F15-F18.

Skoumal, R. J., Ries, R., Brudzinski, M. R., Barbour, A. J., & Currie, B. S. (2018). Earthquakes induced by hydraulic fracturing are pervasive in Oklahoma. Journal of Geophysical Research: Solid Earth, 123(12), 10-918.

Thurber, C., & Eberhart-Phillips, D. (1999). Local earthquake tomography with flexible gridding. *Computers & Geosciences*, *25*(7), 809-818.

Todd, T., & Simmons, G. (1972). Effect of pore pressure on the velocity of compressional waves in low-porosity rocks. *Journal of Geophysical Research*, *77*(20), 3731-3743.

Utsu, T. (1961). A statistical study on the occurrence of aftershocks. *Geophys. Mag.*, *30*, 521-605.

Vasyura-Bathke, H., Dettmer, J., Steinberg, A., Heimann, S., Isken, M. P., Zielke, O., ... & Jónsson, S. (2020). The Bayesian earthquake analysis tool. *Seismological Research Letters*, *91*(2A), 1003-1018.

Visser, R., Kao, H., Dokht, R. M. H., Mahani, A. B., & Venables, S. (2021). A comprehensive earthquake catalogue for northeastern British Columbia: The northern Montney trend from 2017 to 2020 and the Kiskatinaw Seismic Monitoring and Mitigation Area from 2019 to 2020. Geological Survey of Canada.

Wang, B., Kao, H., Yu, H., Visser, R., & Venables, S. (2022). Physical factors controlling the diverse seismogenic behavior of fluid injections in Western Canada. *Earth and Planetary Science Letters*, *589*, 117555.

Wiemer, S., & Wyss, M. (2000). Minimum magnitude of completeness in earthquake catalogs: Examples from Alaska, the western United States, and Japan. *Bulletin of the Seismological Society of America*, *90*(4), 859-869.

Wright, G.N., McMechan, M.E., Potter, D.E.G. (1994): Structure and Architecture of the Western Canada Sedimentary Basin, G.D. Mossop and I. Shetsen (comp.), Canadian Society of Petroleum Geologists and Alberta Research Council, URL https://ags.aer.ca/atlas-the-western-canada-sedimentary-basin/chapter-3-structure-and-architecture , [Last accessed Feb 14, 2024].

Wyss, M., Hasegawa, A., Wiemer, S., & Umino, N. (1999). Quantitative mapping of precursory seismic quiescence before the 1989, M 7.1 off-Sanriku earthquake, Japan. *Annals of Geophysics*, *42*(5).

Yu, H., Harrington, R. M., Liu, Y., & Wang, B. (2019). Induced seismicity driven by fluid diffusion revealed by a near‐field hydraulic stimulation monitoring array in the Montney Basin, British Columbia. *Journal of Geophysical Research: Solid Earth*, *124*(5), 4694-4709.

Zhai, G., Shirzaei, M., Manga, M., & Chen, X. (2019). Pore-pressure diffusion, enhanced by poroelastic stresses, controls induced seismicity in Oklahoma. *Proceedings of the National Academy of Sciences*, *116*(33), 16228-16233.

Zhang, H., & Thurber, C. (2006). Development and applications of double-difference seismic tomography. *Pure and Applied Geophysics*, *163*, 373-403.

Zhao, Y., Jiang, G., Lei, X., Xu, C., Zhao, B., & Qiao, X. (2023). The 2021 Ms 6.0 Luxian (China) earthquake: Blind reverse‐fault rupture in deep sedimentary formations likely induced by pressure perturbation from hydraulic fracturing. *Geophysical Research Letters*, *50*(7), e2023GL103209.

Zoback, M. D., & Gorelick, S. M. (2012). Earthquake triggering and large-scale geologic storage of carbon dioxide. *Proceedings of the National Academy of Sciences*, *109*(26), 10164-10168.

Appendices

Appendix A: Supplemental Table of Seismograph Stations Used In This Study

net	sta	lat	lon	elev	sampling_rate
Sy	1	55.9926719665527	-120.571083068847	768.779418945312	1000
Sy	2	55.9992866516113	-120.558029174804	756.334167480468	1000
Sy	3	56.0095787048339	-120.544212341308	737.860290527343	1000
Sy	4	56.0072593688964	-120.571098327636	749.159057617187	1000
Sy	5	56.0142822265625	-120.557464599609	762.122192382812	1000
Sy	6	55.9998626708984	-120.587219238281	749.684509277343	1000
Sy	7	55.9854431152343	-120.557807922363	777.568908691406	1000
Sy	8	55.9924087524414	-120.545089721679	766.294189453125	1000
Sy	9	56	-120.5263214	765.973266601562	1000
Sy	10	55.9951858520507	-120.518730163574	786.319274902343	1000
Sy	11	55.9856986999511	-120.535690307617	776.988159179687	1000
Sy	12	55.977943	-120.543327	733.077026367187	1000
Sy	13	56.0070838928222	-120.597457885742	753.110961914062	1000
Sy	14	56.0150680541992	-120.607734680175	779.238708496093	1000
Sy	15	56.0145759582519	-120.584091186523	775.427429199218	1000
Sy	16	56.0224342346191	-120.596076965332	801.677978515625	1000

Sy	17	56.0229949951171	-120.571388244628	775.233703613281	1000
Sy	18	56.0289344787597	-120.584068298339	777.991943359375	1000
Sy	19	55.9719772338867	-120.557518005371	689.155334472656	1000
Sy	20	55.9635429382324	-120.564704895019	618.711059570312	1000
Sy	21	55.9777183532714	-120.570953336914	709.091552734375	1000
Sy	22	55.9713172912597	-120.588325500488	690.4921875	1000
Sy	23	55.963321685791	-120.594146728515	681.958129882812	1000
Sy	24	55.9582252502441	-120.584083557128	640.772705078125	1000
Sy	25	55.9854469299316	-120.583847045898	761.562255859375	1000
Sy	26	55.9799690246582	-120.595710754394	718.735839843375	1000
Sy	27	55.9749679565429	-120.609748840332	697.629577636718	1000
Sy	28	55.993309020996	-120.595191955566	778.698181152343	1000
Sy	29	55.9843368530273	-120.608123779296	784.034545898437	1000
Sy	30	55.9775733947753	-120.626556396484	717.916442871093	1000
Sy	31	56.0000457763671	-120.609695443457	761.803100585937	1000
Sy	32	55.9915466308593	-120.620536804199	776.566711425781	1000
Sy	33	55.9849472045898	-120.636451721191	767.586120605468	1000
Sy	34	56.003609	-120.622604	763.172729492187	1000
Sy	35	55.9943313598632	-120.642173767089	811.92578125	1000
Sy	36	56.0025291442871	-120.633094787597	777.959777832031	1000

CN	BCBC	52.372	-126.755	0	100
CN	BLBC	52.044	-119.2439	2357	100
CN	BMBC	56.0449	-122.1336	1092	40
CN	BMTB	56.0451	-122.1332	1099	100
CN	DLBC	58.4372	-130.0272	978	100
CN	EDM	53.223	-113.3497	727	100
CN	FNBB	58.8903	-123.0099	618	40
CN	FNSB	58.8061	-122.7328	440	100
CN	FSB	54.4767	-124.3283	747	100
XL	MG01	56.0548	-120.638	721	100
XL	MG02	55.8668	-120.084	642	100
XL	MG03	55.9122	-120.4414	697	100
XL	MG04	55.9914	-120.338	682	100
XL	MG05	55.8951	-120.3019	795	100
XL	MG06	55.8721	-120.0415	639	100
XL	MG07	55.7836	-120.4024	749	100
XL	MG08	55.8412	-120.8731	722	100
XL	MG09	55.7442	-120.7796	795	100
XL	MG10	55.7229	-120.0633	798	100
XL	MG11	55.86168	-120.11468	657	100
1E	MONT1	55.9102	-120.5865	697	100
1E	MONT2	56.0197	-120.047	642	100
1E	MONT3	56.0058	-120.4539	783	100
1E	MONT4	57.3184	-122.7057	1110	100
1E	MONT5	57.0269	-122.336	1097	100
1E	MONT6	56.1103	-121.017	650	100
1E	MONT7	56.3079	-122.0316	797	100
1E	MONT8	56.0673	-120.7774	695	100
1E	MONT9	55.8039	-120.5388	832	100
1E	MONTA	56.1043	-121.07	651	100

PQ	NAB1	56.76629	-121.25867	754	100
PQ	NAB2	58.59503	-119.16559	646	100
PQ	NBC1	59.65594	-123.82371	421	100
PQ	NBC2	59.77346	-122.48776	486	100
PQ	NBC3	59.63716	-120.66875	452	100
PQ	NBC4	55.6873	-120.6602	815	100
PQ	NBC5	57.52311	-122.67763	1161	100
PQ	NBC6	58.58389	-121.33392	445	100
PQ	NBC7	56.2678	-120.8426	676	100
PQ	NBC8	56.57308	-122.40441	709	100
XL	RU01	56.1451	-120.48004	612	100
XL	RU02	56.13199	-120.18819	611	100
XL	RU03	55.8074	-121.1345	795	100
XL	RU04	55.9614	-121.0388	892	100
XL	RU05	56.1806	-120.7334	606	100
XL	RU06	55.9896	-120.5269	773	100
EO	KSM01	56.020911	-120.553634	773	200
EO	KSM02	55.88666	-120.440672	730	200
EO	KSM03	55.839984	-120.138032	652	200
EO	KSM04	55.77394	-120.64416	705	200
EO	KSM05	55.79272	-120.2098	759	200
EO	KSM06	55.950124	-120.712872	752	200
EO	KSM07	56.001695	-120.920995	803	200
EO	KSM08	56.020422	-120.130554	718	200
EO	KSM09	56.167275	-120.279663	644	200
EO	KSM10	56.082567	-120.784632	715	200
EO	KSM11	55.950124	-120.451232	677	200
EO	KSM12	55.872636	-120.667808	706	200
EO	KSM13	55.978668	-120.318704	683	200